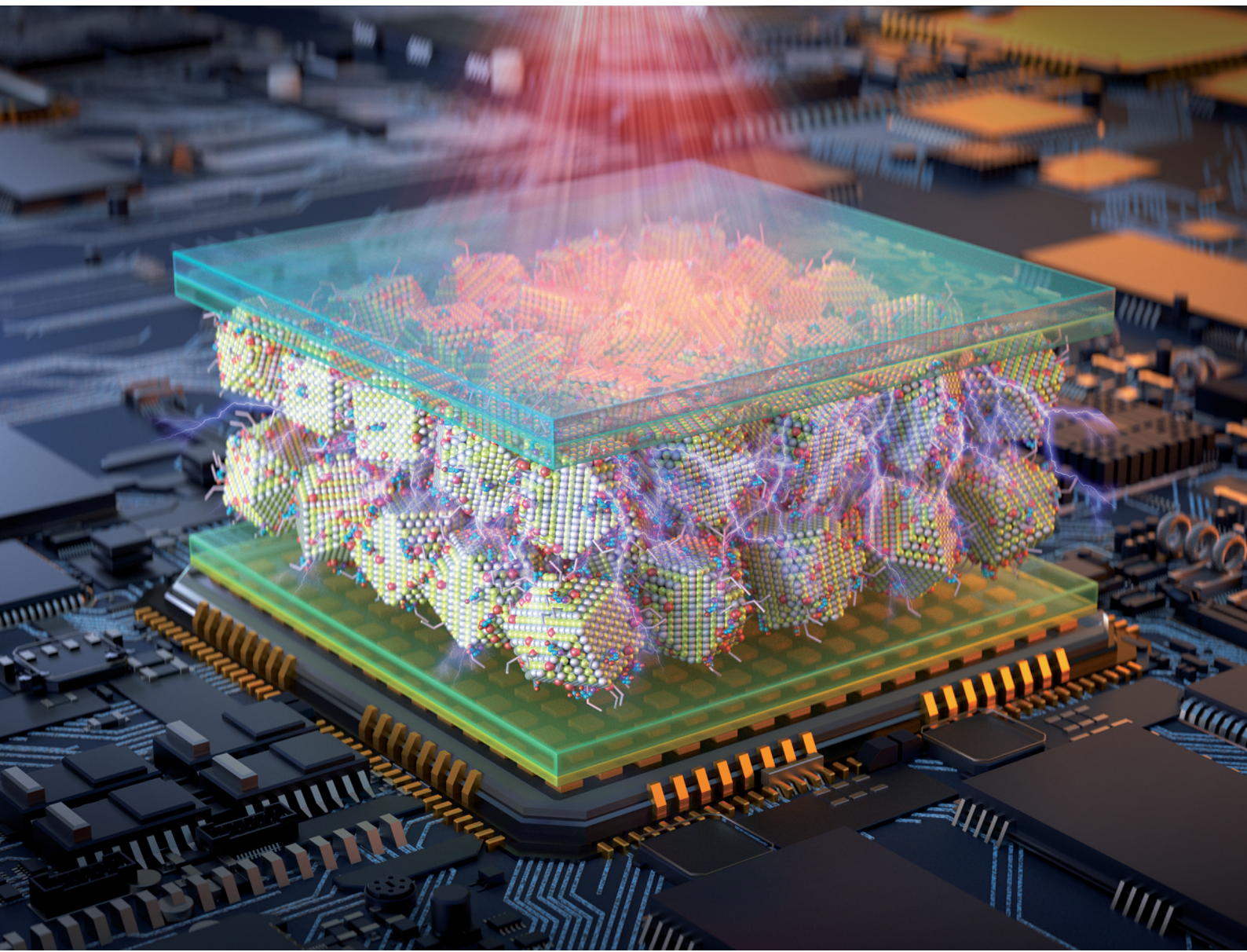


Materials Horizons

rsc.li/materials-horizons



ISSN 2051-6347



Cite this: *Mater. Horiz.*, 2024,
11, 6192

Origin and suppression of dark current for high-performance colloidal quantum dot short-wave infrared photodetectors

Yan Yan, ^{a,b} Hong-Yu Liu, ^c Le Bian, ^{a,b} Yan-Yan Dai, ^c Bo-Ning Zhang, ^c Shuang-Mei Xue, ^{ab} Ye Zhou, ^a Jian-Long Xu ^{*c} and Sui-Dong Wang ^c

The development of cost-effective and highly sensitive short-wave infrared (SWIR) photodetectors is crucial for the expanding applications of SWIR imaging in civilian applications such as machine vision, autonomous driving, and augmented reality. Colloidal quantum dots (CQDs) have emerged as promising candidates for this purpose, offering distinct advantages over traditional III-V binary and ternary semiconductors. These advantages include the ability to precisely tune the bandgap through size modulation of CQDs and the ease of monolithic integration with Si readout integrated circuits (ROICs) via solution processing. Achieving a minimal reverse bias dark current density (J_d) while maintaining high external quantum efficiency is essential for enhancing the light detection sensitivity of CQDs-based SWIR photodiodes to a level competitive with III-V semiconductors. This challenge has garnered increasing research attention in recent years. Herein, the latest advancements in understanding and mitigating J_d in CQDs SWIR photodiodes are summarized. Starting with a brief overview of the material fundamentals of CQDs, the origins of J_d in CQDs photodiodes, including reverse injection from electrode, diffusion/drift currents, Shockley–Read–Hall generation/recombination currents, trap-assisted tunneling, and shunt/leakage currents, are discussed together with their latest research progresses about strategies adopted to suppress J_d . Finally, a brief conclusion and outlook on future research directions aimed at minimizing J_d and retaining high photoresponse of CQDs SWIR photodiodes are provided.

Received 17th August 2024,
Accepted 15th October 2024

DOI: 10.1039/d4mh01094a

rsc.li/materials-horizons

Wider impact

Solution-processed thin-film photodetectors have garnered significant attention due to their capability of monolithical integration with silicon-based complementary metal-oxide-semiconductor readout circuits. This integration offers the potential to overcome the cost and resolution constraints inherent in compound semiconductor infrared focal plane arrays. Notably, colloidal quantum dots (CQDs) have emerged as promising candidates for this purpose, offering distinct advantages over traditional III-V binary and ternary semiconductors. Consequently, significant advancements have been achieved in the development of CQDs-based SWIR photodiodes and state-of-the-art SWIR imagers, paving the way for future advancements in this field. Dark current of a photodiode is defined as any current generated under an applied reverse bias voltage in the absence of light. For most applications, minimizing the CQDs SWIR dark current density (J_d) is crucial to improve key figures of merits. The topic of J_d of CQDs SWIR photodiodes have gained increasing attention in recent years, but the reports and results are scattered in the literature. It is the purpose of this paper to provide an overview to summarize the existing articles on this topic, and to discuss its current status and future research directions about how to minimize J_d and retaining high photoresponse of CQDs SWIR photodiodes.

1 Introduction

1.1 Short-wave infrared light detection

Going beyond visible, infrared light is a specific range of the electromagnetic spectrum, located between visible light and microwave. Categorized based on atmospheric transmission characteristics, infrared light is further divided into short-wave infrared (SWIR, 1–3 μm), mid-wave infrared (MWIR, 3–5 μm), and long-wave infrared (LWIR, 8–14 μm). Among them, the SWIR band can maintain high transmittance in haze

^a State Key Laboratory of Radio Frequency Heterogeneous Integration (Shenzhen University), Shenzhen, Guangdong 518060, P. R. China.
E-mail: yanyan@szu.edu.cn

^b College of Electronics and Information Engineering, Shenzhen University, Shenzhen, Guangdong 518060, P. R. China

^c Institute of Functional Nano & Soft Materials, Jiangsu Key Laboratory for Carbon-Based Functional Materials & Devices, Soochow University, Suzhou, Jiangsu, 215123, P. R. China. E-mail: xujianlong@suda.edu.cn

conditions owing to the wavelength region located in the lower region of the peak absorption of water vapor and carbon dioxide and the weak scattering effect of suspended particles such as dust and smoke in the atmosphere. Notably, the 1.4–2.5 μm SWIR region, serving as a critical atmospheric window in infrared detection, exhibits significant advantages and has emerged as an important band in the detection field.^{1,2} On the one hand, compared to visible light detection, deep penetration depth in haze conditions and high sensitivity to “night glow” radiation makes it easier to distinguish objects, and thus has been widely used in gas sensing, autonomous driving, machine vision and remote sensing.^{3,4} On the other hand, in comparison to LWIR and MWIR, the SWIR band boasts a narrower diffraction limit, facilitating the capture of finer image details and superior visual clarity.⁵ In addition, SWIR detection is less susceptible to environmental thermal noise owing to its higher photon energy compared to MWIR and LWIR. Consequently, SWIR detectors can operate stably with a reasonable signal-to-noise (SNR) ratio in high-temperature environments, minimizing reliance on intricate cooling systems for noise reduction.^{6,7} This not only simplifies the imaging system and reduces fabrication costs, but also significantly improves the reliability of the system. Presently, SWIR detection technology has exhibited great application potential and profound practical significance in military fields like target recognition, missile warning, and precision strike tasks,^{8–11} as well as in civilian applications such as machine vision, medical healthcare, autonomous

driving, and artificial intelligence.^{12–15} Fig. 1a shows the visible and SWIR images acquired for different scenes/applications, indicative of deep penetration depth and high sensitivity of SWIR imaging over visible imaging.¹⁶

1.2 Innovation of SWIR photodetectors

In the realm of commercial SWIR photodetectors, binary and ternary bulk III-V materials, particularly InGaAs and InAs, have emerged as the preferred choice.^{20–22} Their appeal stems from an optimal bandgap, a high SWIR absorption coefficient, high carrier mobility, a low dielectric constant, and superior material stability.²³ Notably, InGaAs SWIR detectors stand out due to their high external quantum efficiency (80–90%) and sensitivity (specific detectivity reaching 10^{13} – 10^{14} $\text{cm Hz}^{1/2} \text{ W}^{-1}$ at room temperature).²⁴ The detection wavelengths region of InGaAs photodetectors is mainly concentrated in the range of 0.9 to 2.0 μm . However, though III-V semiconductor-based SWIR photodetectors exhibit exceptional SWIR detection performances, they require lattice-matched substrates for epitaxial growth and a flip-bonding process for heterogeneous integration with Si-based ROICs (Fig. 1b).¹⁷ During the flip-chip bonding process, indium bump pillars were added between the photodetector array and ROICs for electrical connection, which was completed by bonding the photodetector array onto the ROICs. The epitaxial growth and flip-bonding process dramatically increases the fabrication cost especially for a large imaging array, and also poses substantial challenges in

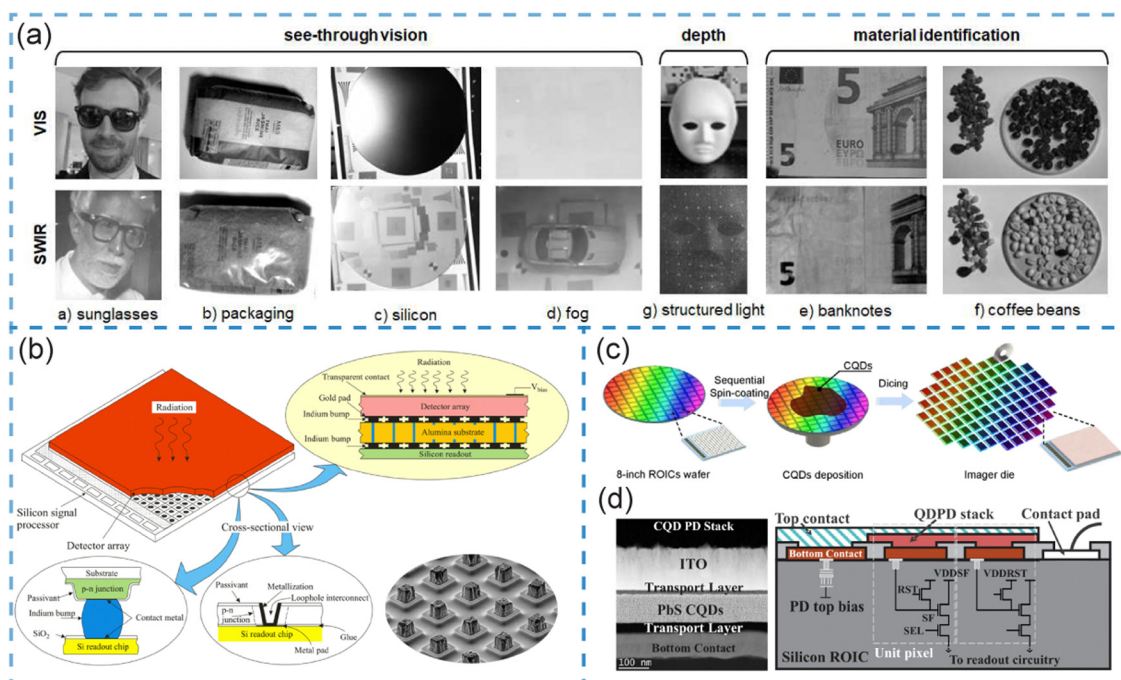


Fig. 1 (a) Images acquired in different scenes/applications for comparison with SWIR and visible imaging. Reproduced from ref. 16 with permission from [Institute of Electrical and Electronics Engineers], copyright [2022]. (b) Hybrid infrared imagers fabricated by a flip-bonding-based process. Reproduced from ref. 17 with permission from [Versital], copyright [2012]. (c) Monolithic integration fabrication process of CQDs with CMOS ROICs. Reproduced from ref. 18 with permission from [American Chemical Society], copyright [2023]. (d) Transmission electron microscopy (TEM) image of a fabricated CQDs SWIR photodiode stack on CMOS ROICs and schematic diagram of the CQDs photodiode stack integration on a ROIC. Reproduced from ref. 19 with permission from [Institute of Electrical and Electronics Engineers], copyright [2021].

imaging resolution (pixel size) and yield in high-pixel-density imaging arrays.^{25,26} It significantly hinders its wide applications in emerging civilian applications, and therefore, the development of low-cost, high-resolution and high-performance SWIR imagers is necessary and still remains challenging.

To extend the array-format of Si CMOS imager, the most efficient strategy is to monolithically integrate SWIR sensing materials with Si ROICs. The first strategy is to epitaxially grow SWIR sensitive materials onto Si, which mainly includes germanium silicon (GeSi) and germanium tin (GeSn) alloy.^{27,28} By fine-tuning the GeSn alloy composition, the detection range can be well modulated and even extend to 3.65 μm , which can fully cover the entire 1–3 μm range of SWIR region.²⁹ Moreover, the GeSn growth process on Si substrates is highly compatible with standard CMOS technology, offering prospects for large-scale and cost-effective manufacturing. This is especially important for constructing low-cost and high-performance SWIR images toward wide applications in civilian fields. However, though progress has been made, GeSn photodetectors still suffer from several critical challenges, including large lattice mismatch (exceeding 4.2%) between Si and GeSn, phase separation and material inhomogeneity at high Sn concentrations, and relatively poor stability of Sn at high temperatures.³⁰ The heterogeneous epitaxial growth of SWIR sensing materials on the complex surface conditions of ROICs, including both oxides and metals, still hinders the achievement of high-performance SWIR photodetectors and imagers. Another feasible and effective strategy is the monolithic integration of SWIR sensing materials with Si ROICs to construct thin-film photodetectors and image sensors. In thin-film photodetectors, all functional layers including the active layer, carrier transport layers, carrier blocking layers and electrodes can be directly fabricated into a pixel stack on top of ROICs with a high or even-unity fill factor. In this process, no epitaxial growth or flip-chip bonding procedure is required, making it possible to achieve low-cost, high-resolution and high-performance SWIR photodetectors. They are getting significant attention as a promising SWIR imaging platform. Among the promising candidates for converting low-energy photons to electric charge carriers, colloidal quantum dots (CQDs) are particularly well suited and have been considered a promising and low-cost SWIR sensitive semiconductor material owing to high potential for pixel size scaling down, high manufacturing throughput and cost-effectiveness.

Typical SWIR sensitive CQDs include PbX (X = S, Se and Te) CQDs, Hg-based CQDs (*e.g.*, HgTe), and environment-friendly CQDs (*e.g.*, Ag₂Te).^{13,31–33} Owing to small Bohr radius and strong quantum confinement effects, the bandgap of PbX CQDs could be precisely modulated by varying the size of CQDs, and the absorption spectrum can fully cover the entire SWIR region, which provides a fundamental foundation for implementation of CQDs SWIR photodetectors.^{34,35} Similar to doping effects in bulk semiconductors, the semiconducting characteristics including n-/p-type doping, doping levels, carrier mobility, carrier concentration and energy band structure can also be precisely modulated by surface chemistry, making it possible to construct various photodetector structures with

optimized photodetection performances. Indeed, PbX CQDs can be mass-produced *via* solution-phase synthesis procedures and then dispersed into highly stable inks, followed by a solution process on top of ROICs (Fig. 1c).¹⁸ After the thickness reached the desired value, the wafer was diced into individual imager chips, which required no hybrid integration process at the chip level by flip-chip bonding. The monolithically integrated pixel, including the photodiode and readout circuit, is shown in Fig. 1d, where the PbS CQDs photodiode is directly fabricated onto the metal pad of the ROICs.¹⁹ Monolithic processing of the CQDs pixels allows us to significantly scale down the pixel size of CQDs imagers compared with flip-chip integrated image sensors, as exemplified by the recent demonstration of a pixel pitch down to 1.62 μm for a 12-inch SWIR imager wafer.³⁶

With extensive efforts in the last decade, significant progress has been made in the photodetection performance of CQDs SWIR photodetectors, benefiting from innovations in CQDs synthesis, defect passivation, device structure design, and pixel optimization. The CQDs SWIR photodetectors stand out among various emerging thin-film SWIR photodetection technologies owing to their superior SWIR photodetection performances and ease of wafer-scale uniform monolithical integration with Si-based ROICs. Fig. 2 shows the scatter plots of photoresponsivity (R) *versus* dark current density (J_d) and specific detectivity (D^*) *versus* wavelength including CQDs SWIR photodiodes^{13,37–57} and other typical material-based SWIR photodiodes such as traditional bulk III–V binary and ternary semiconductors, two-dimensional transition metal dichalcogenides (2D TMDS),^{58–62} conjugated polymers^{63–68} and nanowires.^{69–71} From the R *versus* J_d scatter plot shown in Fig. 2a, it can be clearly seen that the lowest J_d levels of CQDs SWIR photodiodes reported to date are comparable to commercial InGaAs SWIR photodiodes and outperform other emerging technologies. Moreover, the D^* of CQDs SWIR photodiodes reported to date are comparable or superior to other typical SWIR photodetectors (Fig. 2b), offering great potential for further practical applications. Herein, it should be especially noted that D^* values in Fig. 2b are assessed by either using dark current as only source of noise current or adopting measured noise current at different frequencies, and thus such comparison is only for a preliminary reference.

For PbS CQDs photodiodes, two designs have been implemented based on PbS CQDs/metal oxide heterojunctions and PbS CQDs homojunctions. The built-in field at both the heterojunction and homojunction interfaces serves to separate photo-generated carriers and transport them to the electrodes, as illustrated in the band diagram in Fig. 3a.¹⁹ The heterojunction device usually shows relatively low dark current with a typical range of 10^{-8} – 10^{-6} A cm⁻² at a –1 V bias, however, is limited by low photoresponse in the SWIR region.^{41,49,72–81} Inspired by CQDs solar cells, photodetectors based on CQDs homojunctions show much higher photoresponse due to their more suitable energy band alignment and interfacial characteristics. However, the homojunction device typically exhibits high dark current with a typical range of 10^{-6} – 10^{-4} A cm⁻² at –1 V bias, hindering its further practical applications.^{19,37,39,50,52–54,56,82,83}

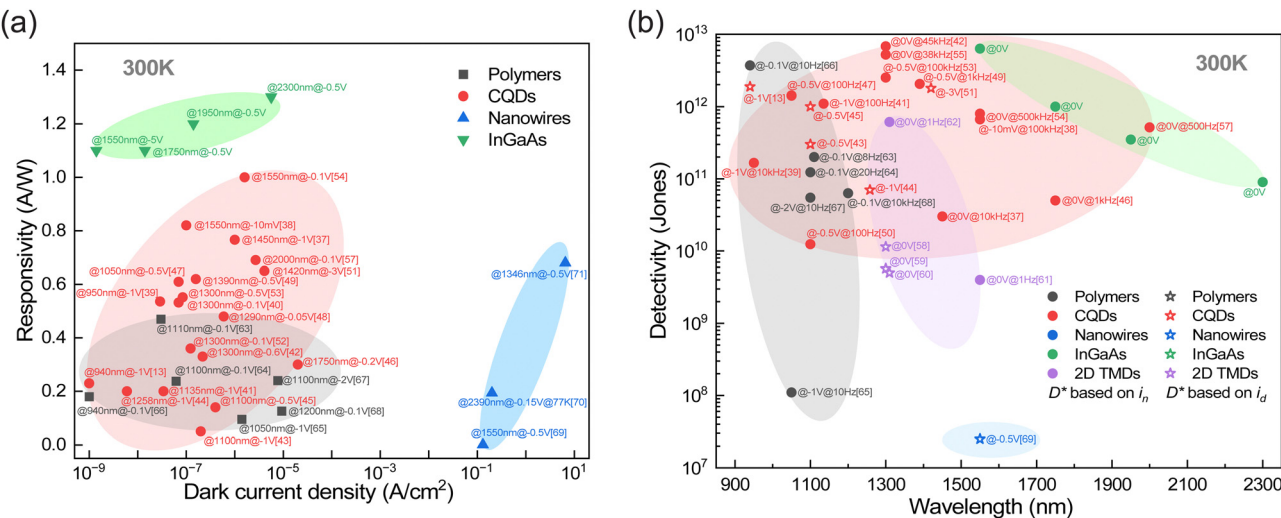


Fig. 2 (a) R versus J_d and D^* versus wavelength scatter plots of CQDs SWIR photodiodes and other typical material-based SWIR photodiodes including traditional bulk III–V binary and ternary semiconductors, 2D TMDs, conjugated polymers and nanowires. Here, the photodetection parameters of CQDs, 2D TMDs, conjugated polymers and nanowires based SWIR photodiodes are extracted from previous literatures,^{13,37–71} while those of III–V ternary InGaAs photodiodes are from the commercial product of Hamamatsu Photonics including G12180-003A, G12181-003A, G12182-003A and G12183-003A.

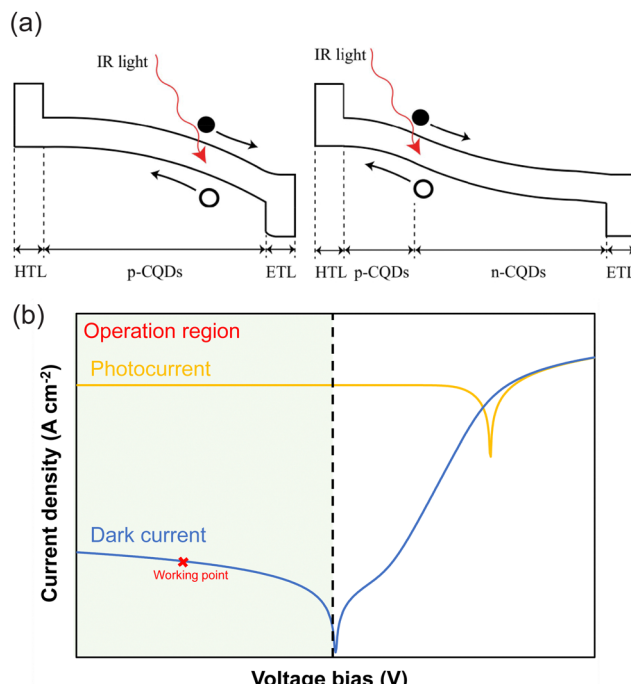


Fig. 3 (a) Illustrated band diagrams of heterojunction and homojunction PbS CQDs photodiodes under a reverse bias and SWIR light illumination. Reproduced from ref. 19 with permission from [Institute of Electrical and Electronics Engineers], copyright [2021]. (b) Typical CQDs photodiode current density versus voltage (J – V) characteristics in a semilogarithmic plot with and without illumination, showing J_d under a given bias voltage.

Therefore, the main challenge for CQDs SWIR photodiodes is how to simultaneously achieve low dark current and high photoresponse, which is mainly limited by the presence of numerous defects in CQDs and the limited carrier mobility

arising from carrier hopping between CQDs. Consequently, optimizing the photodetection characteristics of CQDs SWIR detectors is a current research priority.⁵⁴

1.3 Dark current

Dark current of a photodiode is defined as any current generated under an applied reverse bias voltage in the absence of light, as shown in Fig. 3b. Since SWIR photodiodes are relatively less susceptible to thermal noise, an important contribution to noise current is reverse bias dark current, and thus minimizing J_d is crucial to obtain excellent key figures of merits of photodiodes including linear dynamic range (LDR), signal-to-noise ratio (SNR) and D^* . Elevated dark current can limit the sensitivity of SWIR photodetectors, especially under low-light or elevated temperature conditions. However, solution-processed CQDs SWIR photodiodes still suffer from a relatively high level of J_d compared with commercial III–V bulk photodiodes, which mainly arises from high density of trap states in solution-processed CQDs and at both CQDs/charge transport layer and charge transport layer/electrode interfaces. Moreover, J_d can span several orders of magnitude depending on the device structure and the properties of CQDs. Although enormous efforts including defect passivation of CQDs and employment of hole/electron blocking layers have been made to reduce J_d , it still remains challenging to minimize J_d while retaining high external quantum efficiency for practical applications of CQDs SWIR photodiodes, and also the origin of high J_d in has yet to be fully elucidated.

The topic of J_d of CQDs SWIR photodiodes has gained increasing attention in recent years, but the reports and results are scattered in the literature. It is the purpose of this paper to provide an overview to summarize the existing articles on this topic, and to discuss its current status and future research

directions. Exploration of the origin of J_d and development of specific strategies to reduce J_d from the bulk of this review paper.

2 Materials

2.1 Typical CQDs materials for SWIR detection

Lead chalcogenide (PbX , mainly PbS and PbSe , PbTe to a lesser extent) has been recognized as the most promising CQDs material for SWIR detection. From the fundamental material perspective, PbX exhibits large exciton Bohr radii of 20, 34 and 154 nm for PbS , PbSe and PbTe , respectively,⁸⁴ which allows for quantum size effects even at a large crystal size. Owing to narrow bulk bandgap of 0.37, 0.26 and 0.28 eV for PbS , PbSe , and PbTe ,⁸⁵ the absorption spectrum of PbX CQDs can be modulated over the ultraviolet (UV)-visible-SWIR region (Fig. 4a),⁸⁶ making them promising candidates for active layer in SWIR photodetectors. In contrast to other III-V CQDs, the synthesis of high-quality PbX CQDs is much simpler and more efficient, suitable for upscaled industrialization. Especially, the largely covalent nature of PbS makes it one of the most benign forms for SWIR photodetectors. The bandgap value (E_g) of synthesized PbS CQDs could be well modulated by controlling the CQDs diameter (d), and the fitted curve between E_g and d is shown in Fig. 4b.⁸⁷ It follows the following formula:⁸⁷

$$E_g = 0.41 + \frac{1}{0.0252d^2 + 0.283d} \quad (1)$$

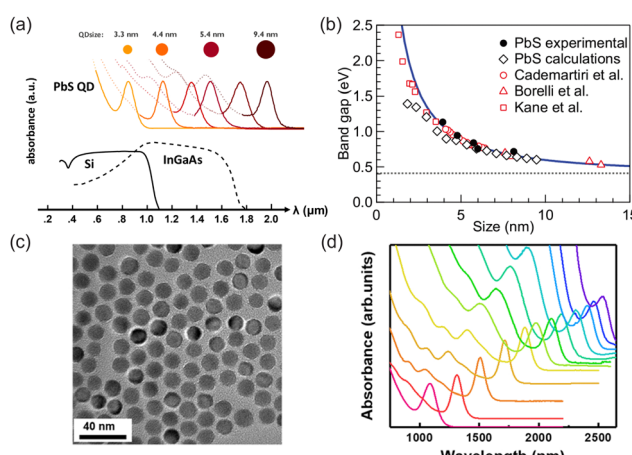


Fig. 4 Size-tunable PbS CQDs. (a) Quantum size effects in PbS CQDs allowing the absorption spectra extending 2.0 μm , outperforming existing Si and InGaAs technologies. Reproduced from ref. 86 with permission from [Institute of Electrical and Electronics Engineers], copyright [2021]. (b) Relationship between PbS CQDs bandgap and size including theoretical calculation and experimental results from different groups. Reproduced from ref. 87 with permission from [American Chemical Society], copyright [2009]. (c) TEM images of ultra-large PbS CQDs with an absorption peak at 2460 nm. Reproduced from ref. 88 with permission from [American Chemical Society], copyright [2019]. (d) Absorption spectra of PbS CQDs with an absorption peak ranging from 1100 to 2600 nm. Reproduced from ref. 88 with permission from [American Chemical Society], copyright [2019].

It can be clearly seen that E_g decreases with the increase of d , and thus large-size PbS CQDs should be synthesized toward SWIR detection applications. This also allows us to determine the diameter directly from E_g , avoiding a lengthly TEM analysis for each synthesized sample. The absorption peak of PbS CQDs has been extended to be over 2500 nm, which can almost cover the entire SWIR region. Dong *et al.* reported ultra-large PbS CQDs with an average diameter of 15.3 nm and a size dispersity lower than 10%, extending the first exciton absorption peak to 2500 nm, as shown in Fig. 4c and d.⁸⁸ The resulted broadband heterojunction photodetectors with an external quantum efficiency (EQE) of 25% at 2100 nm were obtained.

Except for PbX CQDs, mercury telluride (HgTe) CQDs have also emerged as a compelling low-cost candidate for SWIR photodetectors due to its narrow energy transition capabilities and versatile spectral tunability.⁸⁹ Different from HgS and HgSe CQDs showing intraband transition, HgTe CQDs usually exhibit interband electronic transitions upon optical excitation, since their Fermi levels are within the bandgap. Their first band edge optical features can span an incredibly wide range from the visible to the THz range, which directly stems from their semimetallic bulk nature.^{90–92} Moreover, surface chemistry modification for HgTe CQDs has been well developed, and this maturity in surface chemistry allows for precise control and manipulation of electrical properties of CQDs including CQDs coupling, doping level and charge transport behaviors.^{93,94} Significantly, similar to PbX CQDs, the energy levels of semiconducting HgTe CQDs can be well modulated by ligand engineering or doping, which also provides a platform for designing different device structures of photodiodes and phototransistors. Furthermore, the high air stability of HgTe CQDs enables material processing in air ambient while retaining their photoconductive properties.⁹⁵ Benefiting from extensive studies on synthesis methodology and energy level alignments optimization in recent years,^{96,97} dramatic improvements in HgTe -based SWIR and MWIR photodetectors have been achieved.

However, heavy metals of Pb and Hg are *Restriction of Hazardous Substance* (ROHS) regulated elements, which impose major regulatory concerns and impede their employment in consumer electronics. In 2024, a novel synthesis protocol of heavy-metal free silver telluride (Ag_2Te) CQDs was developed and successfully applied in high-performance SWIR photodiodes, as shown in Fig. 5.⁹⁸ In the synthesis protocol, silver-oleylamine and tellurium-thiol complexes were used as Ag and Te precursors for hot-injection. The absence of phosphine results in high stability of Ag_2Te CQDs in crude solution for hours under heating without showing Ostwald ripening, enabling fine modulation of CQDs size by controlling the precursor supply. The resulted Ag_2Te CQDs photodetector exhibits a spectral range of 350–1600 nm with a specific detectivity over 10^{12} Jones, -3 dB bandwidth over 0.1 MHz and LDR over 118 dB.

2.2 Synthesis and size engineering of PbX CQDs

PbX CQDs can be synthesized by a variety of reported methods,^{99–102} among which the most common approach is

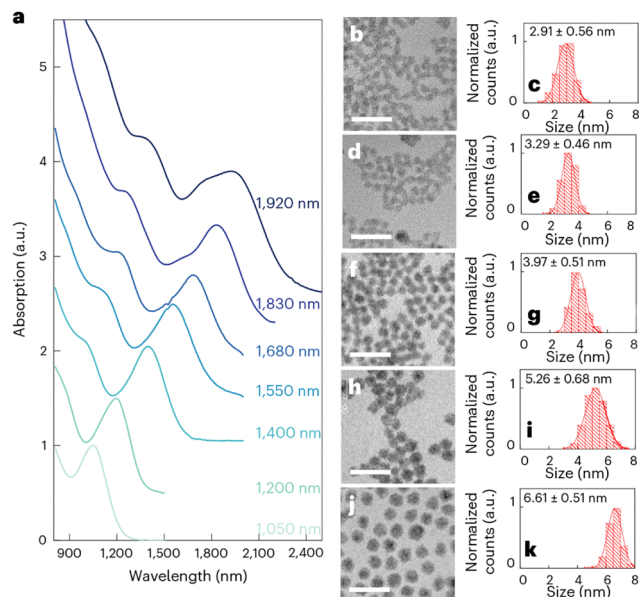


Fig. 5 Size-tunable Ag₂Te CQDs. Reproduced from ref. 98 with permission from [Springer Nature], copyright [2024]. (a) Absorption spectra of Ag₂Te CQDs with various sizes. (b)–(k) TEM images and their size distribution histograms of Ag₂Te CQDs with an absorption peak at 1310, 1430, 1520, 1750 and 1940 nm. Scale bar: 20 nm.

hot injection route pioneered by Hines and Scholes.¹⁰¹ Fig. 6a shows the apparatus setup for a typical hot injection reaction to produce PbS CQDs.¹⁰³ The lead precursor was firstly prepared by dissolving the lead source [*e.g.*, lead oxide or lead acetate] into a non-coordinating solvent such as 1-octadecene in the presence of a coordinating ligand [*e.g.*, oleic acid (OA), oleylamine, or octylamine], which was heated and maintained at a desired temperature. Then, the sulfide precursor was rapidly injected into the lead precursor solution. A burst nucleation event will create a plethora of little occur with gradual decrease of monomers that subsequently grow into large CQDs by further depleting the solution of precursor species,^{104–107} as shown in Fig. 6b. The growth process can be quenched by rapid cooling of the reaction system. Recently, various PbS CQDs synthesis protocols with excellent monodispersity and passivation have been developed by introducing novel lead sources [including Pb(AC)₂ and PbX₂ (X = Cl, Br, I)], sulfide sources (including S and ZnS), changing the amount of OA ligands and altering growth kinetics and thermodynamics during the synthesis.^{100,108–110}

How to obtain high-quality large-size PbX CQDs is crucial for SWIR photodetectors. Commonly, the CQDs diameter can be tunable by adjusting the injection temperature and reaction time in the CQDs synthesis process. The first exciton peaks for PbS CQDs synthesized at different temperatures and growth time are depicted in Fig. 6c.¹⁰⁴ Increasing the injection temperature would decrease the supersaturation, and thus create fewer nuclei and result in larger size of CQDs. Extending the growth time can also enlarge the size of CQDs. Even altering the ligand type is also effective in tuning nucleation rates and thus size of PbS CQDs.¹⁰³ Besides, Dong *et al.* reported a feasible strategy to grow ultra-large PbS CQDs with an

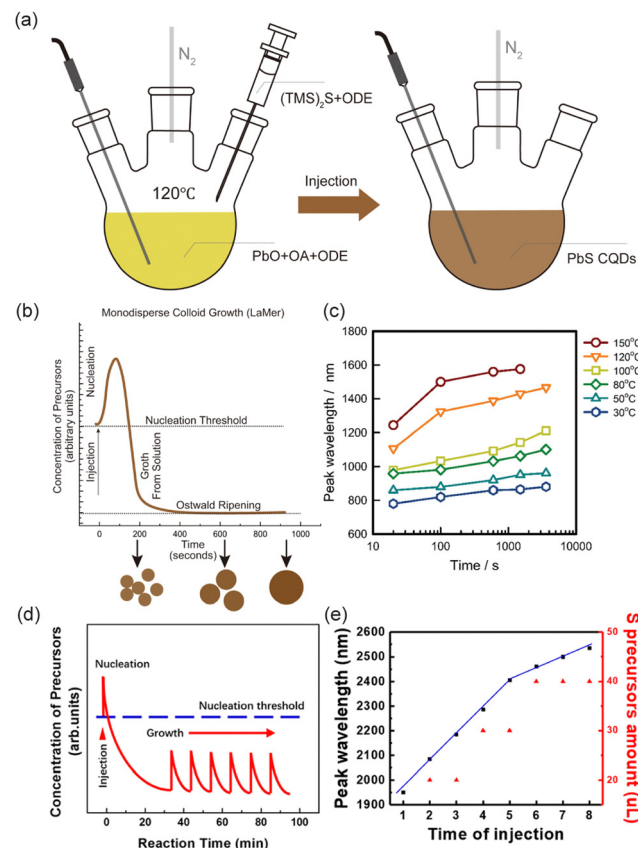


Fig. 6 Synthesis protocol of PbS CQDs using a hot-injection strategy. (a) Scheme of a hot injection reaction apparatus setup for synthesis of PbS CQDs. Reproduced from ref. 103 with permission from [American Institute of Physics], copyright [2023]. (b) Change of PbS precursor with the reaction time during a hot injection reaction, showing the nucleation and growth stage of monodisperse PbS CQDs according to the LaMer model. Reproduced from ref. 103 with permission from [American Institute of Physics], copyright [2023]. (c) Relationship between first exciton peak wavelength of PbS CQDs and the reaction time of period under various reaction temperatures. Reproduced from ref. 104 with permission from [Royal Society of Chemistry], copyright [2017]. (d) Illustration of the two-step synthesis process for ultra-large PbS CQDs. Reproduced from ref. 88 with permission from [American Chemical Society], copyright [2019]. (e) First exciton peak wavelength and added sulfur precursor versus times of injection in the above two-step synthesis procedure of ultra-large PbS CQDs. Reproduced from ref. 88 with permission from [American Chemical Society], copyright [2019].

absorption peak at 2500 nm by multiple injections, using PbS seed crystals with an absorption peak at 1960 nm (Fig. 6d).⁸⁸ The peak wavelength of PbS CQDs increases with the time of injection, where the required sulfur source for each injection increases with the number of injections to maintain the growth of CQDs (Fig. 6e). The authors pointed out that the size of initial seed crystals, time of injection and amount of sulfur source in each injection were of great importance to determine whether uniform large-size PbS CQDs could be successfully synthesized with excellent charge transport and optoelectronic properties.

2.3 Ligand exchange of PbX CQDs

As discussed above, the PbX CQDs synthesized using the hot injection method are usually passivated with long-chain OA

ligands. For active layer applications in photodetectors, the PbX CQDs films should exhibit high electrical conductivity for transport of photo-generated carriers. To achieve this goal, insulating long-chain organic ligands should be replaced with short and/or ionic ligands. There are two common methods for ligand exchange on the surface of CQDs: layer-by-layer solid-state ligand exchange (SSLE) and solution-phase ligand exchange,

and the procedures of these two methods are shown in Fig. 7a.¹¹¹ In the SSLE process, the PbS-OA film was firstly prepared, followed by immersing in the solution with short ligands. The short ligands spontaneously diffuse into the solid-state film to replace the long-chain ligands, which was repeated several times to achieve the desired thickness. Such method is universal and easy to perform, and have been widely adopted for PbX SWIR photodetectors.

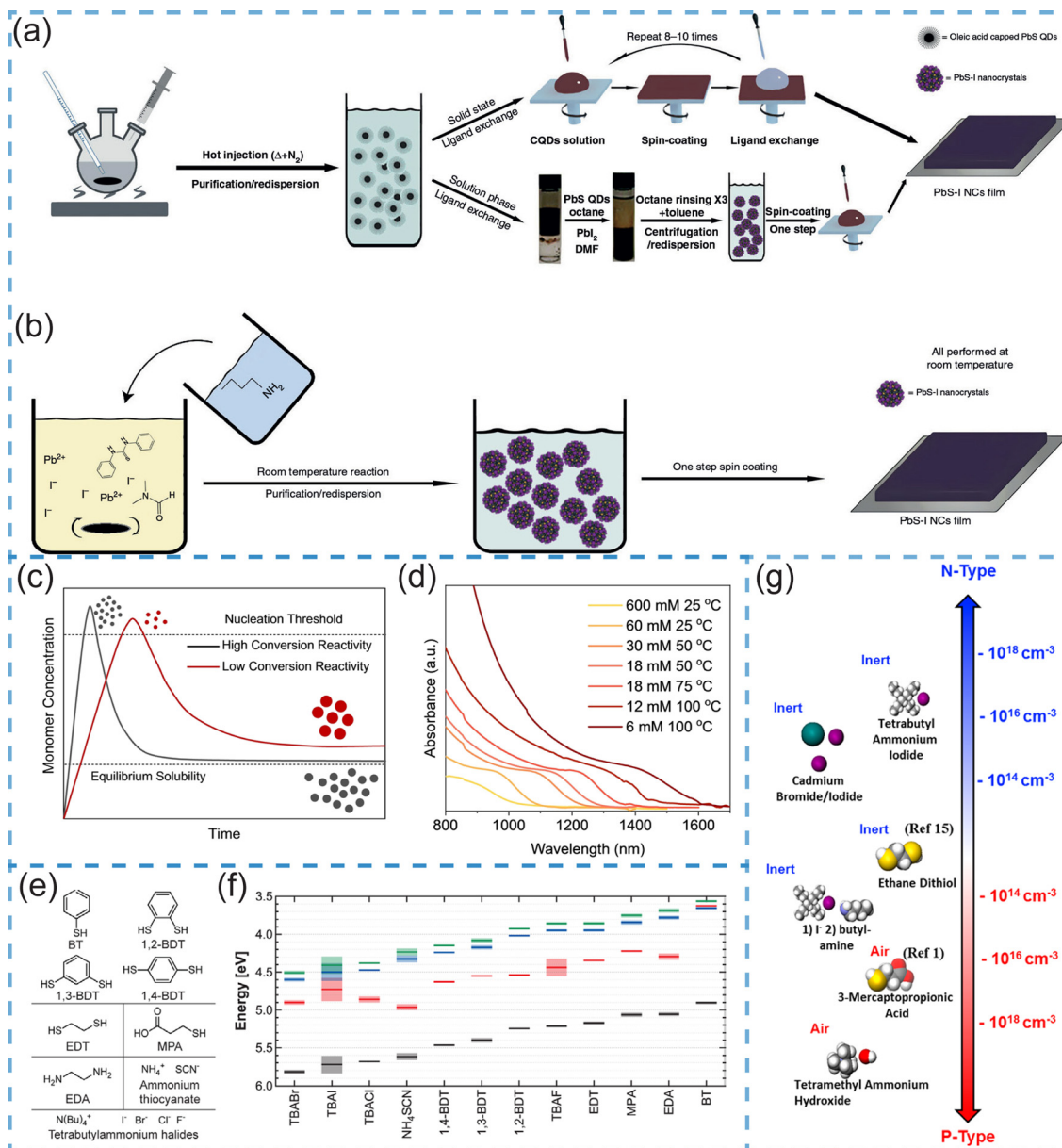


Fig. 7 Ligand exchange in PbS CQDs. (a) Schematic diagram of conventional two-step ligand exchange process including solid-state ligand exchange and solution-phase ligand exchange processes. Reproduced from ref. 111 with permission from [Springer Nature], copyright [2019]. (b) Schematic diagram of newly developed one-step direct synthesis of iodide capped PbS CQDs inks. Reproduced from ref. 111 with permission from [Springer Nature], copyright [2019]. (c) LaMer model for the one-step direct synthesized PbS CQDs inks, showing the effect of precursor conversion kinetics on the size of final CQDs. Reproduced from ref. 113 with permission from [John Wiley and Sons], copyright [2023]. (d) Absorption of one-step direct synthesized PbS CQDs inks under various reaction concentrations and temperatures. Reproduced from ref. 113 with permission from [John Wiley and Sons], copyright [2023]. (e) Chemical structures of the short-chain ligands commonly adopted for exchange with OA in PbS CQDs. Reproduced from ref. 114 with permission from [American Chemical Society], copyright [2014]. (f) Energy level diagrams of PbS CQDs exchanged with different short-chain ligands shown in (e). Reproduced from ref. 114 with permission from [American Chemical Society], copyright [2014]. (g) Effects of short-chain ligand and treatment atmosphere on the doping levels of PbS CQDs. Reproduced from ref. 115 with permission from [American Chemical Society], copyright [2012].

However, the non-uniform exchange and volume shrinkage usually result in film cracks, high defect density and energetic disorder, making it challenging to achieve higher photodetection performances in a wafer scale. In addition, the SSLE process is tedious and time-&cost-consuming, greatly hindering its industrial production.¹¹²

To overcome limitations of the SSLE process, the solution-phase ligand exchange process was developed and have been widely applied in PbX CQDs SWIR optoelectronic devices. In such a process, the ligand was exchanged in a solution phase to obtain high-concentration CQDs ink, followed by spin-coating one time to achieve the desired thickness film (Fig. 7a).¹¹¹ Compared with SSLE method, the homogeneous reaction in the solution-phase results in more thorough and uniform ligand exchange on the surface of CQDs, and also the ink solvent component and concentration is easier to manipulate. Nowadays, PbX CQDs photodetectors with highest photoresponsivity values are almost based on solution-phase ligand exchange process. However, the complex ligand exchange process usually results in the defect regeneration problems, which significantly hinders the photodetection performance enhancement. At the same time, such ligand exchange process greatly limits the synthesis yield in one batch (usually in the milligram range), making it difficult for scalable industrial production. More importantly, the CQDs ink can remain stable within several minutes, which is difficult to meet requirements of practical applications. Therefore, it is necessary to develop stable semiconducting PbX CQDs inks with desired ligand type and concentration on CQDs surface and also low defect concentration.

In 2019, Wang *et al.* developed a one-step synthesis strategy to directly prepare I-passivated PbS CQDs by combining CQDs synthesis and ligand exchange (Fig. 7b),¹¹¹ which can significantly simplify the preparation of CQDs films. In the synthesis process, metal halide (PbI_2) and *N,N*-Diphenylthiourea (DPhTA) were used as lead and sulfide source, respectively. PbI_2 and DPhTA were dissolved in dimethyl formamide (DMF) to obtain the precursor, and butyl amine (BA) was injected into the solution to directly synthesize I-passivated PbS CQDs. This method enables the *in situ* iodide passivation of PbS CQDs and the fabrication of thick films without ligand exchange, which significantly reduces the processing steps and the costs from more than 16 dollars g⁻¹ to lower than 6 dollars g⁻¹. Based on these one-step synthesized halide capped PbS (PbS-I) CQDs, photoconductor-type devices show a high detectivity of 1.4×10^{11} Jones in the near-infrared region. Later in 2023, they revealed the detailed reaction mechanisms of one-step direct synthesis PbS CQDs (Fig. 7c) and realized larger size tunability of PbS CQDs inks with absorption region extending to the SWIR region (Fig. 7d).¹¹³ The photodiode-type photodetector utilizing the SWIR PbS inks combine a low J_d of $2 \times 10^{-6} \text{ A cm}^{-2}$ at -0.8 V bias and a high external quantum efficiency (EQE) of 70% at 1300 nm, compared to or superior to previously reported state-of-the-art PbS CQDs SWIR photodetectors using SSLE or solution-phase ligand exchange process.

Except for enhancing carrier transport, another important role of ligand exchange is to modulate the band structure and

doping levels of CQDs films since the electronic properties of CQDs are critically dependent on the surface chemistry. This allows us to modulate the energy levels of CQDs by introducing different ligands on CQDs surface. Fig. 7e shows the chemical structures of 12 most common adopted ligands employed for replacing OA for higher electrical conductivity, including thiols [benzenethiol (BT), 1,2-, 1,3-, and 1,4-benzenedithiol (1,2-BDT, 1,3-BDT, and 1,4-BDT)], 1,2-ethanedithiol (EDT), and 3-mercaptopropionic acid (MPA)], a primary amine [1,2-ethylenediamine (EDA)], ammonium thiocyanate (SCN), and halides [tetrabutylammonium iodide (TBAI), bromide (TBABr), chloride (TBACl), and fluoride (TBAF)].¹¹⁴ The energy levels of PbS CQDs (with the absorption peak at 963 nm) after exchanged with these different ligands are measured by photoemission and absorption spectra and shown in Fig. 7f.¹¹⁴ A shift of energy levels by up to 0.9 eV between different chemical ligand treatments can be obtained, matching well with the atomistic density functional theory calculation results. Even between chemically similar ligands, the shift of energy levels can also reach 0.2 eV. This arises from different surface dipoles induced between CQDs and different ligands. Furthermore, different ligand treatments of CQDs can also result in n/p-type behaviors and different doping levels of CQDs, as shown in Fig. 7g.¹¹⁵ Usually, halide ligands including TBAI, CdI₂ and CdBr₂ induce n-type doping in CQDs, while thioils including MPA, EDT and 1,2-BDT induce p-type doping in CQDs. It should also be noted that ligand exchange atmosphere (air or inert) has significant effects on doping levels of CQDs. The surface-chemistry-mediated band structures and doping levels allow us to predictably modulated electronic properties of CQDs films and optimize the energy level structure of CQDs photodetectors, which is consistent with bulk materials (in bulk materials such as Si, Ge, InGaAs, etc., the band structure and doping levels can be modulated by adjusting the doping element and concentration).

2.4 Traps in PbS CQDs

As demonstrated in recent research progress, the photodetection performances of CQDs SWIR photodetectors, however, still fall short of what could be expected theoretically. As with other semiconductor devices, the electrical performances of state-of-the-art CQDs SWIR photodiodes is presently determined to a high degree by the presence of electronic trap states which reduce the effective mobility and act as efficient generation-recombination centers within the bandgap of CQDs.^{116–120} Furthermore, the existence of traps makes it extremely challenging to precisely control the free carrier density and n-type/p-type properties of CQDs.¹²¹

Recently, both theoretical and experimental studies have revealed the origin of trap states of CQDs, as shown in Fig. 8a.¹¹⁷ In analogy to their bulk counterparts, trap states in CQDs are typically associated with deep-level electronic states located within the bandgap of individual CQDs (*i.e.* in-gap trap state model). The electronic mid-gap states in individual CQDs mainly arise from physical surface defects including surface vacancies, additional atoms, uncoordinated surface atoms, Pb-Pb formation, etc.^{105,122–124} However, recent theoretical computational studies show that even nonstoichiometric CQDs generally tend to exhibit defect-free

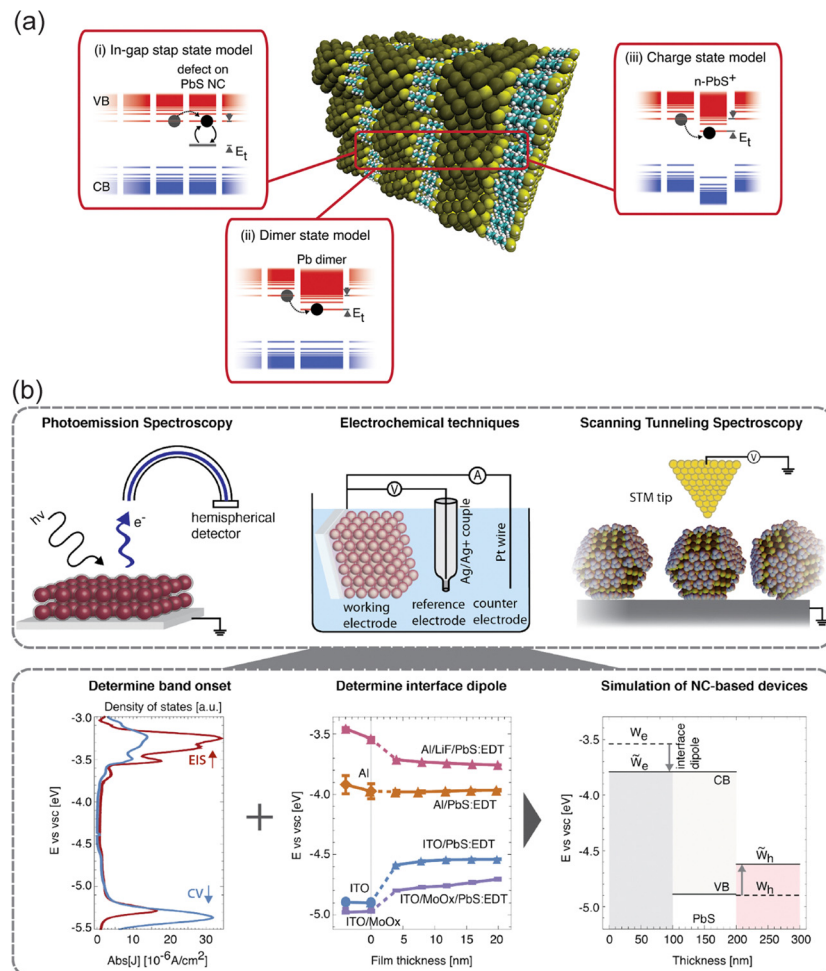


Fig. 8 Traps in CQDs. (a) Schematic diagram of the models of electronic trap state formation in the bandgap including (i) in-gap trap state model, (ii) dimer state model and (iii) charge state model. Reproduced from ref. 117 with permission from [American Chemical Society], copyright [2020]. (b) Experimental techniques to probe the electronic structures and thus trap state information in CQDs including photoemission spectroscopy, electrochemical voltammetry and scanning tunneling spectroscopy. Reproduced from ref. 118 with permission from [American Chemical Society], copyright [2020].

bandgaps.¹²⁵ Until now, this model has received the most attention, and various surface defect passivation strategies have been proposed to reduce density of electronic mid-gap states to increase EQE and reduce J_d of CQDs SWIR photodiodes. Two other origins of trap state formation have also been identified and experimentally demonstrated, which can occur simultaneously in the same CQDs film. Firstly, trap states emerge as a result of two CQDs fusing together (*i.e.* CQDs dimers), which is greatly dependent on the synthesis and thin film fabrication steps of solution-processed CQDs. Recently, surface -OH groups have been demonstrated to induce epitaxial CQDs fusion/dimer.^{126,127} The fused CQDs exhibit less pronounced electronic confinement and thus show a smaller bandgap, which can introduce intermediate states within the bandgap. In detail, an electron/hole trap arises from the energy mismatch of conductive/valence band between a CQDs dimer and surrounding non-fused CQDs. Therefore, CQDs fusion or dimerization has also been identified as a trap state formation model (*i.e.* dimer state model). In recent years, the significance of dimer state model (*i.e.* the effects of CQDs fusion/dimer on

photodetection performances) has also received increased research focus. Secondly, trap states can also originate from doped CQDs (*i.e.* charge state model).¹²⁸ Reduction (oxidation) of p-type (n-type) doped CQDs cause the shift of entire electronic band structure with respect to its surrounding non-doped CQDs, also resulting in a hole (or electron) trap. However, the effects of oxidation or reduction of doped CQDs on photodetection performances of CQDs SWIR photodiodes remains relatively unexplored and warrants further investigation.

While the physical origins of trap states in the above three models differ, each provides a plausible explanation for the defect state behaviors observed in device performance, and thus the insights into all three models could enable further improvement of photodetection performances to theoretical values. Owing to strong correlation between trap states and electronic structures, various optical and electronic techniques have been developed to determine the electronic structure in CQDs, which consist of photoemission (or photoelectron) spectroscopy, electrochemical voltammetry and scanning tunneling

spectroscopy (Fig. 8b).¹¹⁸ Full potential of CQDs photodetectors will be fulfilled after full understanding and control of the electronic structure of individual CQDs and also assembled CQDs films.

3 Performance merits of photodetectors

The feature parameters of photodetectors play a crucial role in evaluating device performance and applications. It is worth noting that these feature parameters are intricately linked to the bias voltage for CQDs photodetectors with low carrier mobility and high density of trap states, necessitating an augmentation in bias voltage to induce carrier drift within the device.

3.1 Responsivity and external quantum efficiency

R reflects the response efficiency of photodetectors to optical signals. R is defined as the ratio of the photocurrent to the detected optical power:

$$R = \frac{J_{\text{ph}}}{P_{\text{in}}} \quad (2)$$

In eqn (2), J_{ph} and P_{in} represent the photocurrent density and incident light intensity, respectively. The unit of R is A W^{-1} . EQE, denoted as η , reflects the conversion of the number of absorbed photons to the number of output electrons, and it is closely related to spectral R . It follows the following formula:

$$\eta = \frac{hc}{e\lambda} R \quad (3)$$

In eqn (3), h , c , e and λ represent Planck's constant, the speed of light, the electronic charge, and the wavelength of incident light, respectively. Since h , c , and e are all constants, for simplicity, the equation can be rewritten as:

$$\eta = \frac{1.24}{\lambda} R \quad (4)$$

where λ is measured in μm .

Here, it should be pointed that R and EQE are usually spectrally invariant and should be as high as possible across the entire operational wavelength range.

3.2 Noise equivalent power and specific detectivity

During photodetector operation, apart from receiving optical signals, it also generates some stray signals, referred to as noise, which can deteriorate its sensitivity and accuracy. Hence, noise parameters are paramount considerations in assessing photodetector performance. The noise of photodetectors mainly includes thermal, shot, and $1/f$ noise, and the typical electronic noise spectrum is shown in Fig. 9. Thermal noise stems from the random thermal motion of charge carriers, independent of applied voltage and solely dependent on temperature and resistance. Shot noise arises from the random fluctuation in the number of photons absorbed by the detector, which is proportional to the square root of the dark current. Thermal and shot noises are independent of the frequency, and

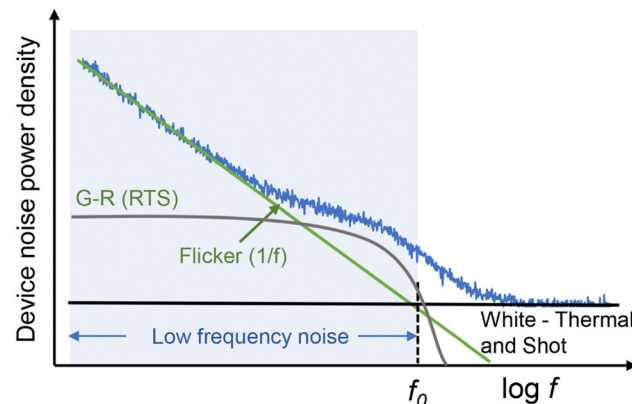


Fig. 9 Typical electronic noise density spectrum in PbS CQDs photodiodes.

thus usually called "white noise". $1/f$ noise, also known as flicker or pink noise, exhibits a power spectral density inversely proportional to frequency at low frequencies. This noise mainly originates from the impurities and defects in semiconductor layers of the device. Until now, two theoretical models have been proposed for how the impurities and defects contribute to the noise: (1) fluctuations in carrier mobility:^{129,130} Impurities and structural defects disrupt the uniformity of the crystal lattice, causing scattering of charge carriers. This scattering leads to variations in carrier mobility, which manifests as noise in the output of devices. (2) Fluctuations in carrier concentration:^{131–133} In addition to mobility fluctuations, defects at interfaces or within the bulk material can act as trap sites. These traps intermittently capture and release carriers, causing fluctuations in the quantity of free carriers. This capture-and-release process introduces additional noise, commonly referred to as generation-recombination noise.

In thin-film CQDs photodetectors, shot noise, thermal noise, and $1/f$ noise coexist, necessitating their careful consideration during design and performance evaluation. In specific applications, photodetectors may exhibit greater sensitivity to noise at particular frequencies. Therefore, in addition to assessing noise levels, it is also necessary to evaluate the spectral characteristics of the noise.

Noise equivalent power (NEP), a pivotal metric for quantifying the sensitivity, reflects the minimum detectable optical power. NEP represents the incident light power yielding a signal-to-noise ratio (SNR) equal to 1, with the unit of watt (W). Its definition is expressed as:

$$\text{NEP} = \frac{i_{\text{n}}}{R} \quad (5)$$

where i_{n} represents the detector noise current.

Since i_{n} scales with device area and R is area-independent in photodiodes, it is unfair to directly compare NEP values of photodiodes with varying device areas. To facilitate the comparison between devices with varying device areas, NEP is normalized to the square root of the device area A_{d} , and defined

as D^* , which is formulated as:

$$D^* = \frac{\sqrt{A_d \Delta f}}{\text{NEP}} = \frac{R \sqrt{A_d \Delta f}}{i_n} \quad (6)$$

where A_d is the effective area of the detector, Δf is the noise bandwidth, and the unit of D^* is $\text{cm Hz}^{1/2} \text{W}^{-1}$ (*i.e.*, Jones).

For noise and D^* measurement, two points should be considered. (i) i_n depends on the applied voltage bias and operating frequency, while R is dependent on wavelength, applied light intensity, and applied bias voltage. Therefore, photodetection performance comparisons between different devices should take these conditions into consideration, and only the comparison between parameters measured and calculated under the same experimental conditions are meaningful. (ii) The contribution of dark current (shot noise, directly calculated from $\sqrt{2qI_d}$) is usually adopted as the only source of noise, leading to an overestimation of specific detectivity. It should be noted that in this case, thermal and $1/f$ noise are ignored, meaning that the calculated D^* represents the maximum theoretical value the device can achieve theoretically. Because it is not always possible to compare D^* values measured under the same experimental conditions, the calculation and comparison of maximum D^* values are preferred. However, accurate evaluation of NEP and D^* should consider all noise sources, not just the contribution of dark current. Therefore, the realistic and accurate noise power spectrum, comprising components such as shot noise, thermal Johnson noise, and $1/f$ noise spectral power density ($i_{1/f}^2(\omega)$), can be represented as:¹³⁴

$$\langle i_n^2(\omega) \rangle_{\text{realistic}} = \left[2q\langle i_d \rangle + \frac{4k_B T}{R_{\text{shunt}}} + i_{1/f}^2(\omega) \right] \Delta f \quad (7)$$

where q is the elementary charge, $\langle i_d \rangle$ is the average dark current, k_B is the Boltzmann constant, T is the temperature and R_{shunt} is the shunt resistance.

3.3 Response/recovery time

Response time (τ_r) and recovery time (τ_f), crucial in evaluating the response speed to optical signals, significantly impact their applications in high-speed imaging, signal processing, and data acquisition. When exposed to or removed from light illumination, a period of time was required for the photodetector to reach a stable state. τ_r is defined as the time for the output signal to rise from 10% to 90% of net photocurrent intensity, while τ_f denotes the time for it to fall from 90% to 10%. These parameters precisely characterize the transient response to optical signals, vital for evaluating and optimizing its performance in specific applications.

3.4 Dark current density

Dark current is a crucial parameter that determines the detection limit of photodetectors, directly influencing their ability to detect ultra-weak optical signals. Typically, the more standardized measure, J_d , is used to evaluate detector performance, with the unit of A cm^{-2} . The lower J_d of a detector, the lower its inherent noise level, thereby enhancing the SNR, LDR and D^* . A higher J_d leads to a lower SNR and thus a decreased sensitivity

to low light intensities. Moreover, a higher J_d results in an increased minimum detectable photocurrent, constraining the LDR, *i.e.*, the operational light intensity range where the photocurrent is linearly correlated to light intensity.

Furthermore, higher J_d increases the noise current and thus decreases D^* . It should be noted that, unlike R , J_d can span multiple orders of magnitude depending on device structure and material properties. During the design and optimization of detector performance, rigorous control of J_d must be taken into account to ensure effective operation under low-light scenarios while maintaining superior imaging quality and signal processing accuracy. Moreover, a high level of J_d usually results in significant challenge in designing ROICs and further imaging accuracy in CQD SWIR imagers. Therefore, from the aspects of photodetection performance optimization, ROIC design and final imaging applications, suppression of J_d is crucial for CQD photodetectors to be competitive with traditional III-V binary and ternary semiconductor SWIR photodetectors and imagers.

4 Origins and intrinsic limit of dark current in CQDs SWIR photodiodes

4.1 Origins of dark current in CQDs SWIR photodiodes

According to the mechanism of current generation, the origins of the dark current can be generally expressed as:

$$J_d = J_{\text{inj}} + J_{\text{TAT}} + J_{\text{SRH}} + J_{\text{DIFF}} + J_{\text{SH}} \quad (8)$$

where J_{inj} refers to reverse injection from electrodes, J_{TAT} represents trap-assisted tunneling (TAT), J_{SRH} is Shockley-Read-Hall (SRH) generation/recombination currents, J_{DIFF} corresponds to diffusion/drift currents, and J_{SH} refers to shunt/leakage currents. For a better understanding, it is useful to categorize these dark current origins into intrinsic and extrinsic factors. Intrinsic factors, such as J_{TAT} , J_{SRH} and J_{DIFF} , arise from the material's fundamental properties like lattice defects and impurities, making them harder to eliminate. Especially, for solution-processed CQDs, passivation of trap states is hard to address and becomes the most significant challenge in the fields, which stems from its synthesis and ligand exchange process in the solution phase. This makes somewhat unique for CQDs SWIR photodiodes that J_{TAT} and J_{SRH} are categorized into intrinsic factors of dark current. Extrinsic factors, such as J_{inj} and J_{SH} , are more easily addressed through design optimizations like incorporating charge-blocking layers and film morphology optimization, and they often result from suboptimal fabrication processes. The entire discussion will focus on the situations occurring in the structure of P-type/Intrinsic/N-type (PIN) photodiodes, and the work condition of reverse bias should also be considered as a premise. The schematic depicting all possible current pathways through a PIN photodiode is illustrated in Fig. 10a.

4.1.1 The reverse injection from electrodes. In a typical PIN photodiode, such as the one depicted in Fig. 10b, the magnitude of the J_d is largely determined by the applied voltage and the reverse injection barrier. Moreover, defects within these

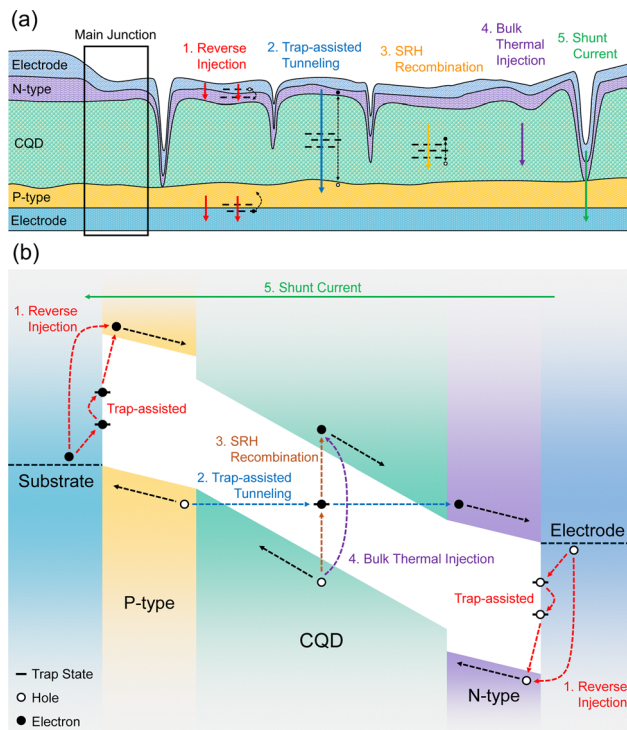


Fig. 10 (a) Schematic illustration of dark current pathways and (b) energy band diagram illustrating origins of dark current in PIN structure photodiodes at a reverse bias, which includes (1) (trap-assisted) reverse injection, (2) trap-assisted tunneling, (3) SRH recombination, (4) bulk thermal injection, and (5) shunt current. Solid arrows indicate the direction of current, while dashed arrows represent the movement of charge carriers (electrons and holes).

barrier layers can create traps that enable minority carrier transitions, leading to thermally activated carrier injection under reverse bias. This process involves carriers jumping from the Fermi level of electrodes to tail of density of states (DOS) in the electron blocking layer (EBL) or hole blocking layer (HBL), a phenomenon well-captured by a model proposed by Arkhipov *et al.*¹³⁵

This model describes a two-step process: the initial carrier injection into the transport layer followed by a certain probability of the carrier escaping to the opposite electrode. It considers key factors such as the image charge effect at the electrode, the energetic site disorder (*e.g.*, interface trap states inherent to the HBL/EBL), and the hopping charge transport mechanism in the CQDs layer. Charge carriers are injected from the Fermi level of electrodes into tail states of DOS of the transport layer. As these carriers move away from the electrode interface, they drift under the electric field towards the opposite electrode, undergoing a diffusive random walk through the disordered energetic landscape. Notably, this injection process is not spatially homogeneous but rather filamentary, driven by spatially fixed states like trap states near the interface between electrodes and transport layers, which create localized pathways for carrier movement.

Based on the assumptions of the Arkhipov *et al.* model, the reverse injection current, J_{inj} , which depends on the charge

carrier density at the metal–semiconductor interface (n_{int}) and the carrier mobility (μ_0) within the semiconductor bulk, can be defined as follows:

$$J_{\text{inj}} = qn_{\text{int}}\mu_0 F \quad (9)$$

In this equation, F refers to the absolute value of the electric field. Considering a Gaussian DOS, the reverse injection barrier Φ_{inj} equals to the effective injection barrier Φ_b minus a term proportional to the thermal equilibrium energy, $\left(\frac{\sigma_i^2}{2k_B T}\right)$, where σ_i represents the energetic disorder at the metal–semiconductor interface. Furthermore, the effective Φ_{inj} is additionally reduced by the image potential barrier lowering $\Delta\Phi_b = \sqrt{\frac{qF}{4\pi\epsilon}}$, where $\epsilon = \epsilon_0\epsilon_r$ denotes the permittivity. The mobility in the zero-field limit and at carrier density in the independent-particle (Boltzmann) regime μ_0 equals the mobility in the infinite temperature limit, μ_0^* , multiplied by a temperature-dependent factor $\exp\left[-C_i\left(\frac{\sigma_b}{2k_B T}\right)^2\right]$, with σ_b the energetic disorder in the bulk of the intermediate layer and $C_i \approx 0.4$ in the extended Gaussian density model.¹³⁶ Consequently, the J_{inj} is expressed as:

$$J_{\text{inj}} = AqN_h \exp\left[\frac{\Phi_b - \left(\frac{\sigma_i^2}{2k_B T}\right) - \Delta\Phi_b}{k_B T} - \mu_0^* \exp\left[-C_i\left(\frac{\sigma_b}{k_B T}\right)^2\right] \frac{V}{L}\right] \quad (10)$$

In this equation, A refers to a dimensionless prefactor considered equal to unity, and N_h represents the volume density of molecular sites between which the hopping takes place. Besides, V and L denotes the bias voltage applied and the thickness of active layer, respectively.

4.1.2 Trap-assisted tunneling current. The TAT current, also known as field-enhanced SRH generation, is a significant component of dark current in CQDs SWIR photodetectors. In this process, generation or recombination of carriers occurs *via* defect states within the bandgap. Initially, an electron is thermally excited from the valence band to a trap state or relaxed from the conduction band to a trap state. The second transition involves ballistic tunneling of the electron into or out of an empty state due to an external electric field, significantly influenced by defects at or near the heterojunction interfaces, as shown in Fig. 10b. The equation of the TAT current can be written as:

$$J_{\text{TAT}} = \frac{q^2 m_t M^2 N_t V}{8\pi\hbar^3 (E_g - E_t)} \exp\left(\frac{-4\sqrt{2m_t}(E_g - E_t)^{\frac{3}{2}}}{3qE_{\max}\hbar}\right) \quad (11)$$

In this equation, m_t stands for the effective tunneling masses, N_t the activated trap density, E_g the bandgap energy, E_t the trap state energy, and E_{\max} the maximum electric field, respectively. Moreover, the trap potential, commonly adopted in infrared detectors, is $M^2 = 10^{-23} \text{ eV}^2 \text{ cm}^3$.

To mitigate TAT, improving the material quality to reduce trap density is crucial. In CQDs photodetectors, deep-level defects typically arise from incomplete passivation during ligand exchange or local CQDs concentration non-uniformities after spin-coating. The influence of band-to-band tunneling (BTBT) is generally not considered because the CQDs layer is relatively thick, resulting in a lower electric field strength.

4.1.3 SRH generation/recombination current. The SRH generation–recombination mechanism is a major source of dark current in reverse-biased CQDs SWIR photodetectors. This temperature-assisted two-step process occurs when an electron is thermally excited from the valence band to a localized state within the bandgap and subsequently transitions from this state to the conduction band, or *vice versa*, as shown in Fig. 10b. The energy exchange occurs *via* phonons, rendering the process temperature-dependent.

Under reverse bias conditions, the carrier concentration in the depletion region is significantly lower than that at equilibrium, resulting in enhanced generation of electron–hole pairs *via* defect states within the bandgap. The thermal excitation of an electron from the valence band to a trap state leaves a free hole in the valence band, which subsequently moves to the electrode by drift or diffusion. Moreover, the trap state energy landscape can be altered by an external field, known as the Poole–Frenkel effect,¹³⁷ which reduces the effective energy required for electrons to escape the trap. Consequently, the SRH generation current increases with the increase of reverse bias due to the greater depletion of carriers and reduced activation energy. Conversely, under forward bias, the carrier concentration is significantly higher than at equilibrium, and recombination predominates over generation. Defect states within the bandgap serve as efficient recombination centers, increasing the recombination current in proportion to the density of these states. The equation of the SRH current can be considered as:

$$J_{\text{SRH}} = qw \frac{\beta_{\text{SRH}} N_t n_i}{2 \cosh \left(\frac{E_t - \sqrt{\frac{q^3 F}{\pi e \epsilon_0}} - E_i}{k_B T} \right)} \quad (12)$$

In eqn (12), the symbol w stands for the thickness of depletion region, β_{SRH} is the SRH recombination rate coefficient, and E_i refers to the mid-gap energy.

The SRH current is characterized by an activation energy typically around half of E_g , indicating the significant role of mid-gap traps. In CQDs photodetectors, the density and distribution of these traps are influenced by surface chemistry and the quality of CQDs passivation. Reducing the density of mid-gap states through improved surface passivation techniques can effectively lower the SRH generation–recombination current.

4.1.4 Diffusion/drift current of the main junction. In the main junction of CQDs SWIR photodetectors, the diffusion and drift current contributes to the overall dark current. This component can significantly impact device performance,

especially under low-light conditions. When the photodiode is reverse-biased, the depletion region expands, enhancing the electric field across the junction. This electric field is crucial for the movement of charge carriers. Thermally generated minority carriers in the neutral regions, with electrons in the p-type region and holes in the n-type region, are driven towards the depletion region by a concentration gradient, as shown in Fig. 10b. This diffusion process, characterized by the diffusion coefficient, is influenced by the material properties and temperature. An exemplary equation of the diffusion current is shown as follows:

$$J_{\text{DIFF}} = n_i^2 \sqrt{q k_B T} \left(\frac{1}{N_a} \sqrt{\frac{\mu_n}{\tau_n}} + \frac{1}{N_d} \sqrt{\frac{\mu_h}{\tau_h}} \right) \left[\exp\left(\frac{qV}{k_B T}\right) - 1 \right] \quad (13)$$

In eqn (13), n_i represents the intrinsic carrier concentration. Besides, N_a denotes the acceptor concentration, N_d the donor concentration, μ_n the electron mobility, μ_h the hole mobility, τ_n the electron lifetime, and τ_h the hole lifetime, respectively.

4.1.5 Shunt/leakage current. In CQDs SWIR photodetectors, shunt or leakage current arises due to cracks or pinholes in the CQDs layer. Additionally, an excessively thin blocking layer can result in direct contact between portions of the electrode and the active layer, creating low-resistance pathways for dark current generation, as shown in Fig. 10a. Shunt currents are particularly problematic as they increase the noise level and degrade the SNR, thus reducing the overall sensitivity of the device. Optimizing the fabrication process and improving material purity are essential strategies to minimize these leakage pathways and enhance the performance of photodetector. The shunt resistance may exhibit temperature dependence, which can have a significant impact on current fitting, particularly when the shunt resistance is relatively low.¹³⁸ In such cases, the current density can be expressed as:

$$J_{\text{SH}} = J_{\text{SH0}} \exp\left(\frac{-E_{\text{SH}}}{k_B T}\right) \quad (14)$$

where E_{SH} is the activation energy of the shunt current, and J_{SH0} is a constant related to shunt resistance. When the shunt resistance is sufficiently large, it can be assumed to be independent of temperature, allowing for a simplification of the model.

Understanding the various mechanisms contributing to the dark current in CQDs SWIR photodetectors is crucial for enhancing their performance. Current research indicates that the primary contributors to reverse dark current in devices are predominantly J_{SH} and J_{TAT} . Particularly under large reverse bias conditions, J_{TAT} can be more dominant due to typically high trap states in CQDs.^{53,55,56} This makes trap-assisted mechanisms somewhat more unique in CQDs devices compared to their bulk counterparts. Addressing these mechanisms through material optimization, defect reduction, and advanced fabrication techniques can lead to significant improvements in device sensitivity and reliability. Future research should focus on developing strategies to mitigate these dark current sources, thereby paving the way for high-performance CQDs

photodetectors suitable for a wide range of infrared sensing applications.

4.2 Intrinsic limit of dark current in CQDs SWIR photodiodes

In the study of SWIR CQDs photodiodes, the intrinsic limit of dark current is critical for optimizing device performance. This limit establishes a baseline to assess deviations from ideal performance. In the most ideal scenario, the radiative saturation dark current, which is the thermal diffusion/drift current at the main junction, defines the theoretical minimum dark current level in a photodiode. This current arises solely from thermal radiation noise due to the interaction between the device and its environment. Analogous to calculating the short-circuit current density in solar cells,¹³⁹ based on the detailed balance principle,¹⁴⁰ the radiative saturation dark current density (J_{rad}) is determined by the overlap between the blackbody thermal photon flux, $\phi(E)$, and the EQE(E), expressed as:

$$J_{\text{rad}} = q \int \text{EQE}(E) \phi(E) dE \quad (15)$$

The function $\phi(E)$ can be derived from the blackbody spectrum.¹⁴¹ Multiplying this by a factor of q and converting it to units of $\text{mA cm}^{-2} \text{ eV}^{-1}$ provides the spectrum over a range of temperatures (Fig. 11a). The simulated EQE spectra of the optical absorption material can be modeled by a function of the form:

$$\text{EQE}(E) = \kappa \frac{G_d}{2} \left[1 + \text{erf} \left(\frac{E - E_g}{\sigma \sqrt{2}} \right) \right] \quad (16)$$

where erf represents the error function, with κ being the constant of proportionality specific to EQE, and G_d representing the volume density. The actual experimental EQE measurements of CQDs is also shown in Fig. 11a. To further understand the influence of EQE spectra on J_{rad} , three variations of the

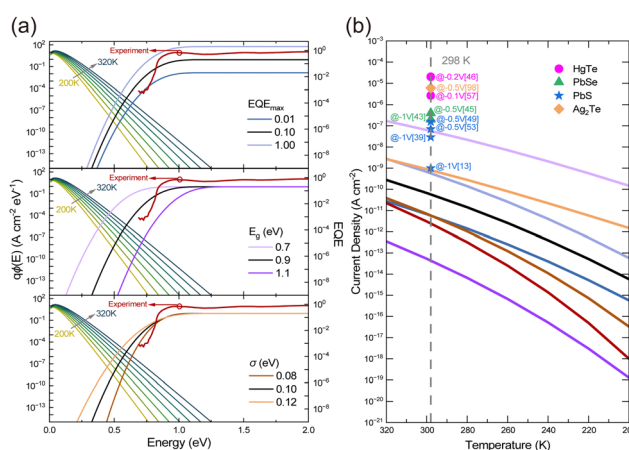


Fig. 11 Intrinsic limit of dark current calculations. (a) Blackbody thermal photon flux $\phi(E)$ with a factor q and simulated EQE spectra with EQEmax , E_g and σ . (b) The temperature-dependent dark current density calculated through eqn (15). The red solid line represents the result of experimental EQE measurements of CQDs. Additional data points represent the dark current density of different materials, including HgTe,^{46,57} PbSe,^{43,45} PbS,^{13,39,49,53} and Ag₂Te,⁹⁸ extracted from previously published literature.

spectra are considered: the maximum EQE magnitude (EQEmax), E_g , and the standard deviation of the Gaussian energy DOS (σ). Obviously, a large EQE contribution at low energies can significantly increase the dark current, which is also heavily influenced by temperature, as shown in Fig. 11b, highlighting the critical role of sub-bandgap states. In experimental measurements, the EQE data exhibits a relatively low dark current density due to measurement limitations, leading to the absence of J_{SRH} . However, in practical devices, the dark current density is often much higher than the intrinsic limit calculated theoretically, primarily due to additional dark current pathways, as previously discussed.^{13,39,43,45,46,49,53,57,98} This indicates considerable potential for device performance optimization, especially through reducing defect state density and improving fabrication processes.

5 Suppression strategies of dark current in CQDs SWIR photodiodes

According to the dark current mechanisms of PIN photodiodes, the dark current can be impeded by designing the band alignment, regulating the intrinsic carrier concentration, optimizing the film morphology and reducing the trap density of functional layers. In addition, interfacial engineering by insertion of modification layer or surface passivation can effectively passivate the interfacial defects, thereby inhibiting dark current associated with the interfacial trap-related carrier generation-recombination process. In this section, we will discuss the different dark current suppression methods and working mechanisms in CQDs PIN photodiodes, which is mainly divided into two parts: one is related to carrier transport layer and the other one is related to CQDs layer.

5.1 Optimizing of the carrier transport layer: energy band, defects and interface

5.1.1 Suppression of reverse carrier injection by optimizing energy band alignment. In PIN structured photodiodes, minority electrons (holes) are injected from high (low) work function electrode into energy states in the tail of the Gaussian DOS of conduction (valence) band of CQDs films. The charge injection rate is expected to be inversely proportional on the injection barrier height, defined as energy difference between conduction (valence) band of CQDs and Fermi level of the high (low) work function electrode in the case of electrons (holes). A higher injection barrier results in a lower dark current for a given applied bias. Therefore, applying a hole/electron blocking layer (HBL/EBL) which provides a higher injection barrier at both electrode/carrier transport layer interfaces is commonly adopted by researchers to suppress the dark current. By matching the energy levels among electrodes, carrier transport layer and active layer, the ideal blocking layer will also facilitate the transport of majority carriers while blocking the injection of minority carriers from electrodes. Thus, the optimized device structure should be electrode/HBL/electron transport layer (ETL)/active layer/hole transport layer (HTL)/EBL/electrode.

Here, most researchers used specific materials to obtain the effect of both blocking the minorities and transporting the majorities as one layer, in order to decrease the fabrication complexity. Moreover, except for blocking of minority carrier injection from electrodes, the high conduction (valence) band levels of HBLs and EBLs make the holes (electrons) generated within the active layer difficult to reach the electrodes through the blocking layer. Therefore, energy level engineering plays an important role in choosing the materials for blocking layer. Simultaneously, the method for depositing blocking layers deserves the same consideration in order not to introduce defects in the functional layer and surface states between the layers.

In 2011, Sarasqueta *et al.* experimentally verified the role of hole/electron blocking layers and compared the blocking effects of various HBLs and EBLs in the indium tin

oxide (ITO)/MoO₃/PbSe CQDs/Al photodiodes, as shown in Fig. 12a-I.⁴³ By introducing HBLs and EBLs to suppress the minority carrier injection from ITO and Al electrodes, J_d was obviously suppressed accompanying with the improvement of photocurrent and thus specific detectivity. Through comparative studies, p-type Poly-TPD and n-type ZnO nanoparticles exhibited higher hole and electron blocking effects (Fig. 12a-II), while ensuring the transportation of photo-generated electrons and holes. Ka *et al.* introduced low-cost solution-processed CuSCN as EBL/HTL of PbS CQDs photodiodes.⁴⁴ Regardless of the electrode material, the topper minimum conduction band contributes to a high energy barrier, preventing the injection of minority electrons from Au electrodes (Fig. 12b-I). The dark current drops about two orders in the resulting devices, reaching 6 nA cm^{-2} under -1 V bias (Fig. 12b-II). The simplified method and attractive performances render

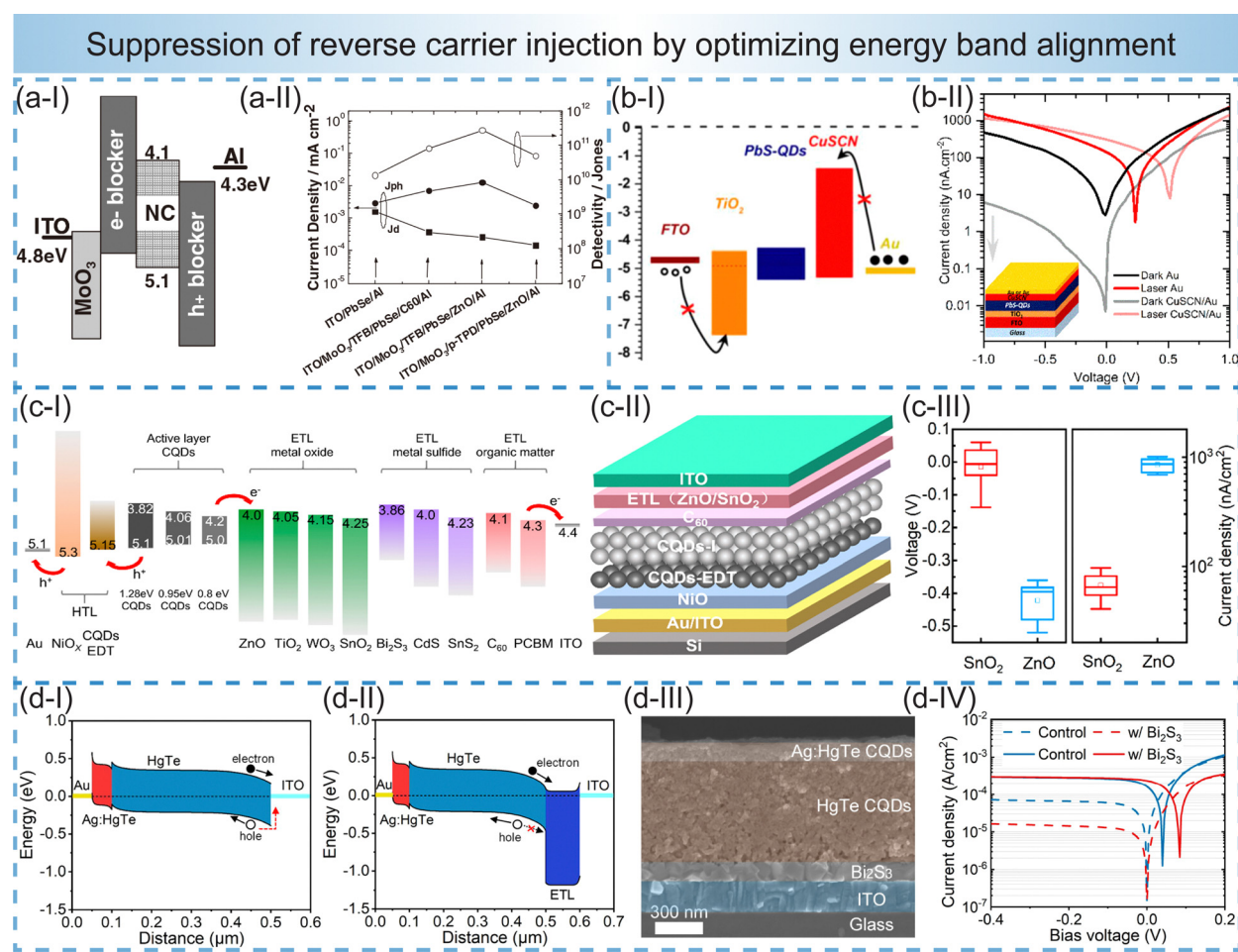


Fig. 12 Energy band alignment optimization of ETLs and HTLs to suppress reverse carrier injection and thus J_d . (a-I) Energy band alignment of photodiodes utilizing EBLs and HBLs. (a-II) J_d and specific detectivity values of photodiodes utilizing different EBLs and HBLs. (b-I) Energy band alignment of photodiodes with CuSCN layer. (b-II) $J-V$ curves of Au and CuSCN/Au photodiodes in dark and under illumination. (c-I) Energy band diagrams of photodiodes utilizing different inorganic and organic ETLs. (c-II) Schematic illustration of Si integrated front-side illuminated PbS CQDs photodiodes utilizing ZnO and SnO₂ ETLs. (c-III) Comparison of voltage and J_d of photodiodes with SnO₂ and ZnO ETLs. (d-I) and (d-II) Energy band diagram of Au/Ag:HgTe/HgTe/ITO photodiodes w/o and w/ Bi₂S₃ ETLs. (d-III) Cross-sectional SEM image of glass/ITO/Bi₂S₃/HgTe CQDs/Ag:HgTe CQDs/Au photodiodes. (d-IV) $J-V$ curves of HgTe CQDs photodiodes w/o and w/ Bi₂S₃ ETLs in dark and under 1550 nm illumination. Figure reproduced with permission from: (a) ref. 43, [John Wiley and Sons], copyright [2011]; (b) ref. 44, [American Chemical Society], copyright [2020]; (c) ref. 38, [American Chemical Society], copyright [2023]; (d) ref. 142, [American Chemical Society], copyright [2023].

CuSCN as a potential candidate of EBLs. Until now, various HBLs and EBLs have been proposed and adopted in PbS photodiodes to simultaneously block the minorities and transport the majorities. The commonly used EBLs include metal oxides (*e.g.*, NiO_x), thiols-capped PbX CQDs and organic materials (*e.g.*, TFB, Poly-TPD, TAPC, CuSCN), while HBLs mainly include metal oxides (*e.g.*, ZnO, TiO₂, WO₃, SnO₂), metal sulfides (*e.g.*, Bi₂S₃, CdS, SnS₂), halide-capped PbX CQDs, and organic materials (*e.g.*, C₆₀, PCBM), as shown in Fig. 12(c-I).^{38,43,44,142,143}

The EBLs and HBLs, especially when deposited on top of the CQDs layer, were mainly fabricated using a solution process due to its fabrication simplicity and negligible damage to the underlying CQDs layer. However, it is challenging for solution-process EBL and HBL layers to ensure excellent crystallization and low defect density in such a low-temperature process (Usually, the PbS CQDs films cannot tolerate long-time annealing process above 100 °C). Starting from this point and also considering higher compatibility with standard CMOS process, Zhang *et al.* demonstrated atomic layer deposition (ALD) as a suitable way for depositing oxide functional layers on top of CQDs layer at low temperature (Fig. 12c-II).³⁸ During the sputtering process, it is possible to import impurity ions in the functional layer and introduce damage to the below CQDs layer, while ALD is a mild strategy to avoid such issues. Zhang *et al.* utilized ALD prepared SnO₂ as the blocking layer here instead of sputtered ZnO. Owing to better aligned energy level and more qualified heterojunction interface prepared from ALD, the SnO₂ device obtained an extremely low J_d of 3.5 nA cm⁻² at -10 mV (Fig. 12c-III). Furthermore, Bi₂S₃ is reported as a new type of ETL/HBL suitable for HgTe CQDs SWIR photodiodes.¹⁴² As shown in Fig. 12d-I, the suitable energy levels of Bi₂S₃, along with their efficient electron extraction efficiency, could simultaneously suppress the reverse minority carrier injection from ITO to HgTe CQDs and enable the transportation of electrons from HgTe CQDs to ITO, which is expected to suppress J_d and improve J_{ph} . The high surface flatness of Bi₂S₃ films also endows the multilayer structure of Au/Ag:HgTe CQDs/HgTe CQDs/Bi₂S₃/ITO photodiodes with qualified heterojunction interface, as shown in Fig. 12d-II. As expected, the integration of Bi₂S₃ ETL/HBL has led to a substantial decrease in J_d , down to as low as 1.6×10^{-5} A cm⁻² at -400 mV (Fig. 12d-III), and a remarkable increase in D^* to approximately 10¹¹ Jones at room temperature.

5.1.2 Interfacial and bulk defect passivation of ETLs and HTLs.

Having suppressed the reverse minority injection by optimizing energy band alignment, J_d of CQDs photodiodes still deviates from the calculated theoretical lower limits to a large extent. One of the main factors responsible for this deviation arises from the interfacial and bulk defects of EBLs and HBLs. As one of the most reported ETL/HBL, ZnO-based PbS CQDs photodiodes still suffer from large J_d and low repeatability, which arise from low crystallinity and high sensitivity of ZnO film surface to oxygen and water molecules. The density functional theory (DFT) calculation results showed that the polar (002) ZnO crystal plane exhibited a much higher adsorption energy of water molecules compared to other

nonpolar planes. Based on the sputtering method, Lu *et al.* obtained the (002)-oriented and high-crystallinity ZnO ETL/HBL, which is beneficial for suppressing water molecule adsorption.⁴⁰ Compared with the sol-gel ZnO device, the sputtered ZnO device exhibited lower J_d , higher J_{ph} , and a faster photoresponse at a reverse bias (Fig. 13a-I). The significantly suppressed J_d mainly results from the suppression of the interfacial TAT process. The electrons in the valence band of p-type PbS CQDs layer can tunnel into the conduction band of n-type ZnO *via* intermediate states within the depletion region, forming trap assisted tunneling (TAT) current (Fig. 13a-II). Thus, the surface passivation in the sputtered ZnO device results in a reduced contribution of TAT current to J_d , thus greatly suppressing J_d . Furthermore, oxygen absorbed at the ZnO NPs surface also creates surface states into which carriers become trapped, resulting in increased trap-assisted carrier diffusion and tunneling, which hinders the extraction of photoelectrons. Ultraviolet (UV) activation has been proved to be effective in removing surface absorbed oxygen molecules and maintaining high photodetection performances.¹⁴⁴ However, UV activation of ZnO NPs is not permanent and diminishes in a matter of minutes (Fig. 13b-I). Additionally, infrared photodiodes cannot be continuously irradiated with UV illumination. Parmar *et al.* confirmed that unfavorable ZnO plane orientations cause oxygen adsorption and demonstrated that ALD-processed ZnO films ZnO films can serve as a UV activation-free alternative.³⁹ The optimized ALD ZnO devices significantly enhance the EQE, reduce J_d , and improve the stability of PbS CQDs SWIR photodiodes, as shown in Fig. 13b-II.

Besides, the critical role of defects in CQDs HTL/EBL and ETL/HBL on J_d is also verified. Zhang *et al.* introduced n-type PbS CQDs armed with a strongly bound ligand, *trans*-4-(trifluoromethyl) cinnamic acid (TFCA), instead of a weakly bound inorganic ligand, TBAI, as a new class of ETL/HBL in homojunction photodiodes (Fig. 13c-I), which combined the advantages of more flexible energy band engineering and surface passivation.³⁷ As a result, the SWIR photodetector realized 66% EQE and 1×10^{-3} mA cm⁻² dark current under -1 V bias. Moreover, TFCA suppressed the bias-induced ion migration inside ETL (Fig. 13c-II), and thus improved the operation stability of photodiodes by 50 times compared to TBAI, resulting in a lower J_d at reverse bias stress (Fig. 13c-III). Wang *et al.* introduced a controlled oxidation process to passivate the defects of PbS-EDT HTL/EBL layer and thus suppress J_d .⁴² This process involves annealing the PbS CQDs by exposing them to air at 90 °C with a relative humidity of 35% and an ambient temperature of 25 °C. The controlled oxidation process led to the surface passivation of PbS-EDT films and suppression of the nonradiative recombination. As a result, the TAT current is significantly suppressed, and the oxides also act as gap fillers for cracks in PbS-EDT films fabricated from an SSLE process, which helps in suppressing ohmic leakage, as shown in Fig. 13d-I. Benefiting from this physical process, J_d greatly decreases from 8159 nA cm⁻² to 218 nA cm⁻², as shown in Fig. 13d-II. Nevertheless, it was also demonstrated that excessive oxidation procedures would lead to a substantial decrease in photocurrent.

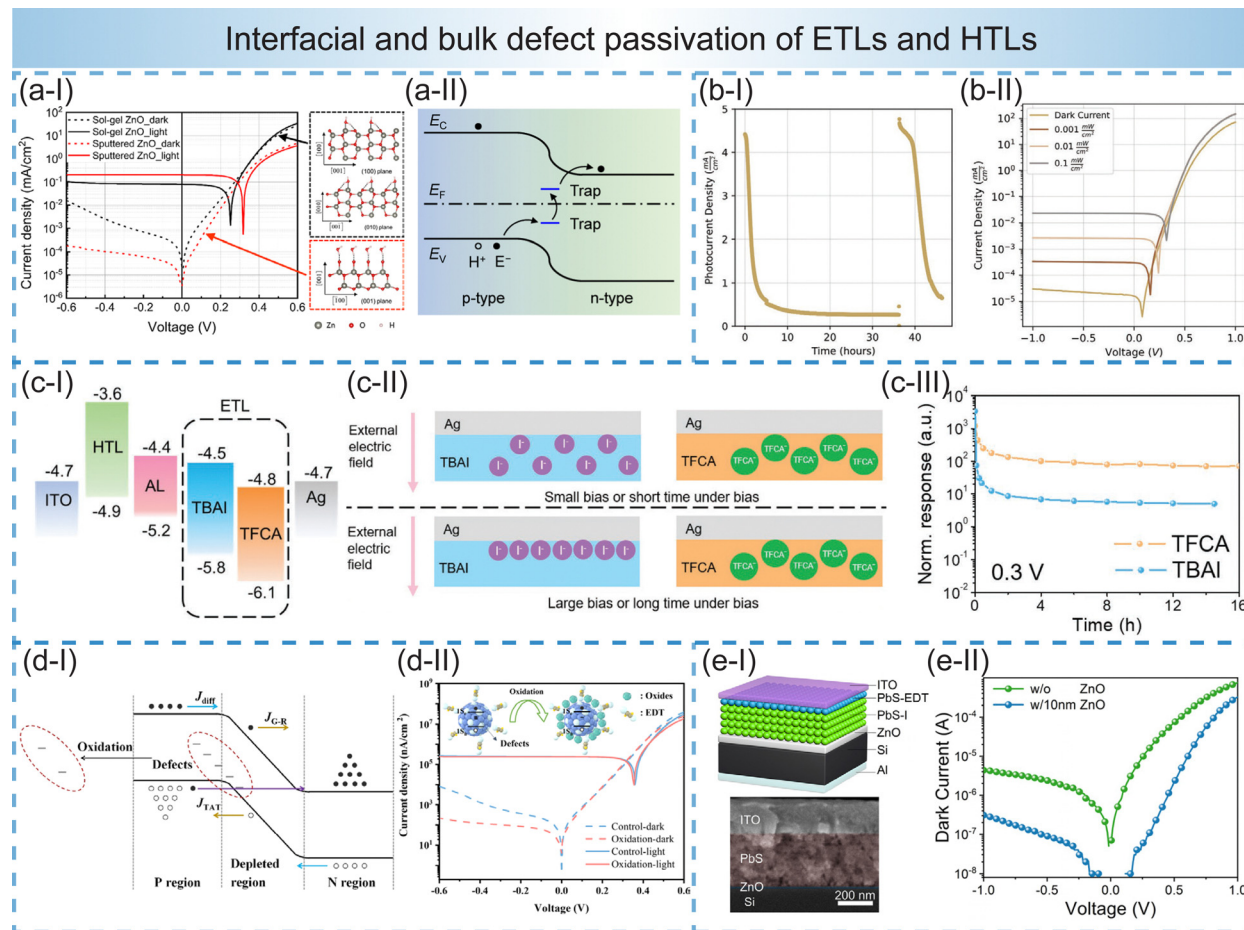


Fig. 13 Interfacial and bulk defect passivation of ETLs and HTLs to suppress defects assisted J_d . (a-I) J - V curves in dark and under illumination of PbS CQDs photodiodes utilizing sol-gel ZnO and sputtered ZnO ETLs. (a-II) Schematics for the mechanism of trap-assisted tunneling current. (b-I) Stability of photocurrent density under constant IR illumination (5 mW cm^{-2}) before and after 37 h UV activation. (b-II) J - V characteristics of ALD ZnO devices in dark and under various illumination intensities. (c-I) Energy band diagram of ITO/HTL/PbS CQDs/ETL/Ag photodiode with PbS-TBAI or PbS-TFCA ETLs. (c-II) Schematics for ion migration at Ag/TBAI and Ag/TFCA interfaces under large and long-time external electric field bias. (c-III) J_d versus time curves of photodiodes utilizing PbS-TBAI and PbS-TFCA ETLs at -0.3 V bias. (d-I) Schematics for the mechanisms of defect assisted tunneling and generation-recombination current. (d-II) J - V curves in dark and under illumination of PbS CQDs photodiodes before and after oxidation. (e-I) Schematic diagram and cross-sectional SEM image of Si integrated front-side illuminated ITO/PbS-EDT/PbS-I/Si/Al photodiode w/o and w/ ZnO ETLs. (e-II) J_d - V curves of Si integrated photodiodes w/o and w/ ZnO ETLs. Figure reproduced with permission from: (a) ref. 40, [American Chemical Society], copyright [2023]; (b) ref. 39, [John Wiley and Sons], copyright [2022]; (c) ref. 37, [John Wiley and Sons], copyright [2022]; (d) ref. 42, [American Chemical Society], copyright [2023]; (e) ref. 145, [American Institute of Physics], copyright [2020].

Thus, it is significantly important to find an appropriate level of oxidation for PbS-EDT films to achieve a balance between dark current and photocurrent.

The construction of the heterojunction structure between PbS CQDs films and bulk Si paves another way to achieve CMOS-compatible SWIR photodiodes. However, the fabrication of high quality CQDs:Si van der Waals heterojunctions is always hindered by the large energy offset between Si and small bandgap PbS CQDs, as well as a high density of surface defects on the Si surface. Xiao *et al.* inserted a layer of solution-processed ZnO nanoparticles between Si and PbS CQDs to simultaneously introduce energy barriers between Si and PbS CQDs and passivate the surface dangling bond of Si (Fig. 13e-I), resulting in suppressed reverse minority injection from Si to PbS CQDs.¹⁴⁵ As a result, the Si:CQDs heterojunction

photodetector shows a significantly reduced J_d at reverse bias (Fig. 13e-II), which results in a high D^* of 4.08×10^{11} Jones at -0.25 V bias at room temperature.

5.1.3 Improving the carrier transport layer/electrode interface. As discussed above, reverse carrier injection from electrodes to function layers could cause an increase in J_d , which could be suppressed by optimizing the energy band alignment and carrier transport layer/PbS CQDs interfacial defect passivation.¹⁴⁶ Besides, the defects located at the carrier transport layer/electrode interface may provide hopping sites for reverse minority injection from electrode to ETL/HTL and thus contribute greatly to J_d , which should be taken into account for further suppression of J_d . In 2023, Gong *et al.* introduced carrier-selective layers LiF and MoO_x with adaptive energy levels at the carrier transport layer/electrode interfaces to suppress

the reverse injection from electrodes and improve the extraction of photo-generated carriers.⁴⁷ Along with other interface engineering strategies, a low J_d of about 70 nA cm^{-2} at -0.5 V and a high D^* up to $1.42 \times 10^{12} \text{ Jones}$ at 1100 nm was obtained in the optimized ITO/LiF/SnO₂/PbS-halide/PbS-malonic-acid (MA)/MoO_x/Au photodiodes. In 2024, Wang *et al.* also used a LiF modification layer at the PbS-EDT/Au interface to lower dark current from a different physical mechanism (Fig. 14a-I).⁴⁸ It was found that the diffusion of Au atoms into both HTL and active layers is one of the factors that cause the instability of PbS CQDs photodetectors that use Au electrodes. On the basis of this, a surface strategy that applies a self-assembled island-like layer LiF between electrode and CQDs layers was proposed, successfully restraining the diffusion of Au and passivating the interfacial defects. Inferior photodetection performances of devices utilizing thicker or thinner LiF layer indicate a possible tunneling mechanism of carrier transport in the LiF layer (Fig. 14a-II). The suppressed Au atom diffusion and interface passivation caused by LiF significantly reduces J_d when the LiF thickness reaches 6 nm, as shown in Fig. 14a-III. As a result, an improvement of D^* from 1.8×10^{12} to $4.8 \times 10^{12} \text{ Jones}$ at the first exciton peak of 1290 nm was accomplished.

Except for introducing an additional interfacial layer, Yang *et al.* demonstrated how the self-formed AlO_x at the ZnO nanoparticles/Al interface dramatically reduced J_d of the PbS CQDs SWIR photodiodes with an ITO/NiO_x/PbS CQDs/ZnO/Al structure (Fig. 14b-I).⁴⁹ In pristine PbS CQDs photodiodes, there exists a large number of defect-induced states at the ZnO/Al interface,^{148,149} which provide hopping sites for hole injection from Al electrode under a reverse bias, leading to a relatively high J_d . However, after post-exposure to dry air, these interfacial defects were thoroughly passivated by the formation of an interfacial AlO_x layer, which reduced the defect-induced hopping sites for minority hole injection from the electrode, consequently lowering J_d (Fig. 14b-II). The resulting device showed an impressively low J_d of $1.58 \times 10^{-7} \text{ A cm}^{-2}$, a high R of 0.62 A W^{-1} at 1413 nm , and a remarkably high D^* of $2.05 \times 10^{12} \text{ Jones}$ at -0.5 V bias. Moreover, the suppression of J_d is highly dependent on the duration of dry air post-exposure (e.g., coverage of AlO_x layer at ZnO/Al interface), as illustrated in Fig. 14b-III.

For front-side illuminated photodiodes, a transparent conducting electrode (TCE) is always required, with ITO being the most commonly adopted SWIR TCE. However, during the ITO sputtering process, the high-energy particles and plasma emission can irreversibly damage the bottom functional layer,¹⁵⁰ potentially creating alternative leakage pathways and consequently increasing J_d . To reduce contact resistance and minimize damage effects of ITO sputtering, Lee *et al.* inserted a 10 nm *N1,N1'*-(biphenyl-4,4'-diyl)bis(*N1*-phenyl-*N4,N4*-di-*m*-tolylbenzene-1,4-diamine) (DNTPD) layer with 5% F6TCNNQ doping between DNTPD HTL and sputtered ITO TCE (Fig. 14c-I).⁸³ Along with optimized energy band alignment (Fig. 14c-II), J_d of CQDs photodiodes with a pixel size of $10 \times 10 \mu\text{m}^2$ was minimized to be as low as $1.1 \times 10^{-7} \text{ A cm}^{-2}$ at -3 V bias (Fig. 14c-III). Furthermore, instead of adding an extra layer, solution-processed

TCEs were fabricated on top of photodiodes instead of the sputtered ITO TCE, thereby entirely avoiding the damage effects during the ITO sputtering process. Owing to their high electrical conductivity, suitable energy levels and high chemical stability, two-dimensional (2D) MXenes are often used as an alternative TCE to replace brittle, expensive and diffusive ITO.¹⁵¹ Di *et al.* proposed a solution-processed interface design of 2D Titanium Carbide (Ti₃C₂) MXene and PbS CQDs layers for photodiodes with an MXene/PbS-EDT/PbS-I/ZnO/Au structure (Fig. 14d-I).¹⁴⁷ The solution-processed interface engineering of MXene/PbS CQDs remarkably decreases the interface defect density by forming a low-defect interface, which can be explained by avoiding the bombardment effects of sputtering and covering the surface cracks (Fig. 14d-II). A low J_d of $0.2 \mu\text{A cm}^{-2}$ at -0.5 V bias voltage is thus achieved (Fig. 14d-III). Meanwhile, the device exhibits a LDR of 140 dB, a -3 dB bandwidth of 0.76 MHz, and a D^* of $5.51 \times 10^{12} \text{ cm W}^{-1} \text{ Hz}^{1/2}$ in the self-powered mode.

5.2 Optimizing of the CQDs photoactive layer: thickness, morphology, material composition and trap states

As previously mentioned, optimizing the photoactive layer of photodiodes, alongside adjusting the device's energy level structure and transport layers, is crucial for reducing dark current and enhancing photodetector performance. By minimizing the defect density, regulating the layer thickness, improving the interfacial uniformity, and optimizing the contact with transport layers, significant reduction in dark current and improvement in photoresponse can be achieved. These adjustments bring the device closer to an ideal photodiode.

5.2.1 Thickness optimization. The thickness of the active layer in CQDs photodiodes significantly influences both light absorption and carrier transport properties. Thicker active layers enhance light absorption by providing a longer photon path length, thereby increasing exciton generation and device sensitivity. However, an excessively thick active layer usually cannot be fully depleted, resulting in increased recombination losses and decreased carrier lifetime since carriers are required to travel longer distances in such thick active layers, ultimately reducing the overall efficiency. In contrast, thinner active layers facilitate more efficient carrier transport by reducing the travel distance, thus minimizing recombination events and the dark current. However, if the layer is too thin, it compromises light absorption, resulting in a lower photocurrent. Therefore, optimizing the active layer thickness is essential to achieving a balance between adequate light absorption and efficient carrier transport,¹⁵² ultimately enhancing the performance of the device. Several studies have indicated that a finely tuned thickness can significantly improve device performance. In 2022, Gong *et al.* discovered that the thickness of CQDs layers is directly proportional to the density of interface traps and inversely proportional to the minimum bulk trap density.⁵⁰ In this study, they fabricated the photodiode devices with an ITO/SnO₂/PbS-1-ethyl-3-methylimidazolium iodide (EMII)/PbS-EDT/Au structure. They found that at a specific PbS-EMII layer thickness of 136 nm, the device reached a balance point where both trap density and J_d were minimized (Fig. 15a-I). The J_d was

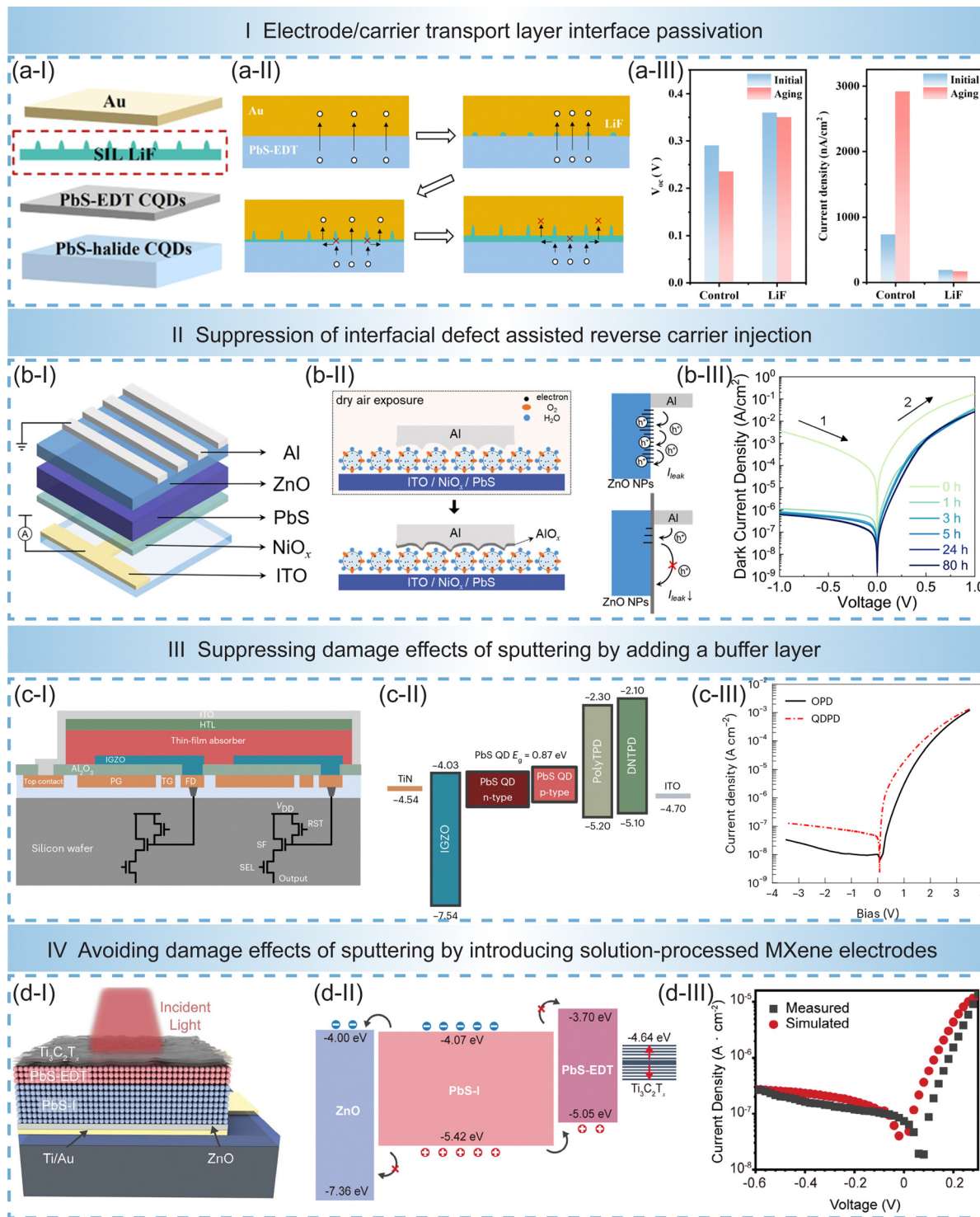


Fig. 14 Improving the electrode/carrier transport layer interface to suppress J_d . (a-I) Schematic illustration of the interfacial SIL LiF layer. (a-II) Schematic diagram of carrier transport in SIL LiF layer with different LiF thicknesses. (a-III) V_{oc} and J_d of initial and aging photodiodes w/o and w/interfacial SIL LiF layer. (b-I) Device structure of an ITO/NiO_x/PbS/ZnO/Al photodiode. (b-II) Schematic illustration of self-formed interfacial AlO_x layer at the ZnO/Al interface and mechanism of J_d suppression. (b-III) $J-V$ curves of photodiodes before and after post-exposure to dry air for different periods of time. (c-I) Simplified diagram of two adjacent pixels in the top view. (c-II) Energy band diagram of the PbS CQDs SWIR photodiodes. (c-III) J_d-V curves of organic and CQDs photodiodes developed in this imager chip. (d-I) Device structure of the top-illuminated PbS CQDs photodiode integrated on Si utilizing solution-processed MXene TCEs instead of sputtered ITO. (d-II) Energy band diagrams of the corresponding photodiode. (d-III) Experimental and simulated J_d-V curves. Figure reproduced with permission from: (a) ref. 48, [American Chemical Society], copyright [2024]; (b) ref. 49, [American Institute of Physics], copyright [2023]; (c) ref. 83, [Springer Nature], copyright [2023]; (d) ref. 147, [John Wiley and Sons], copyright [2024].

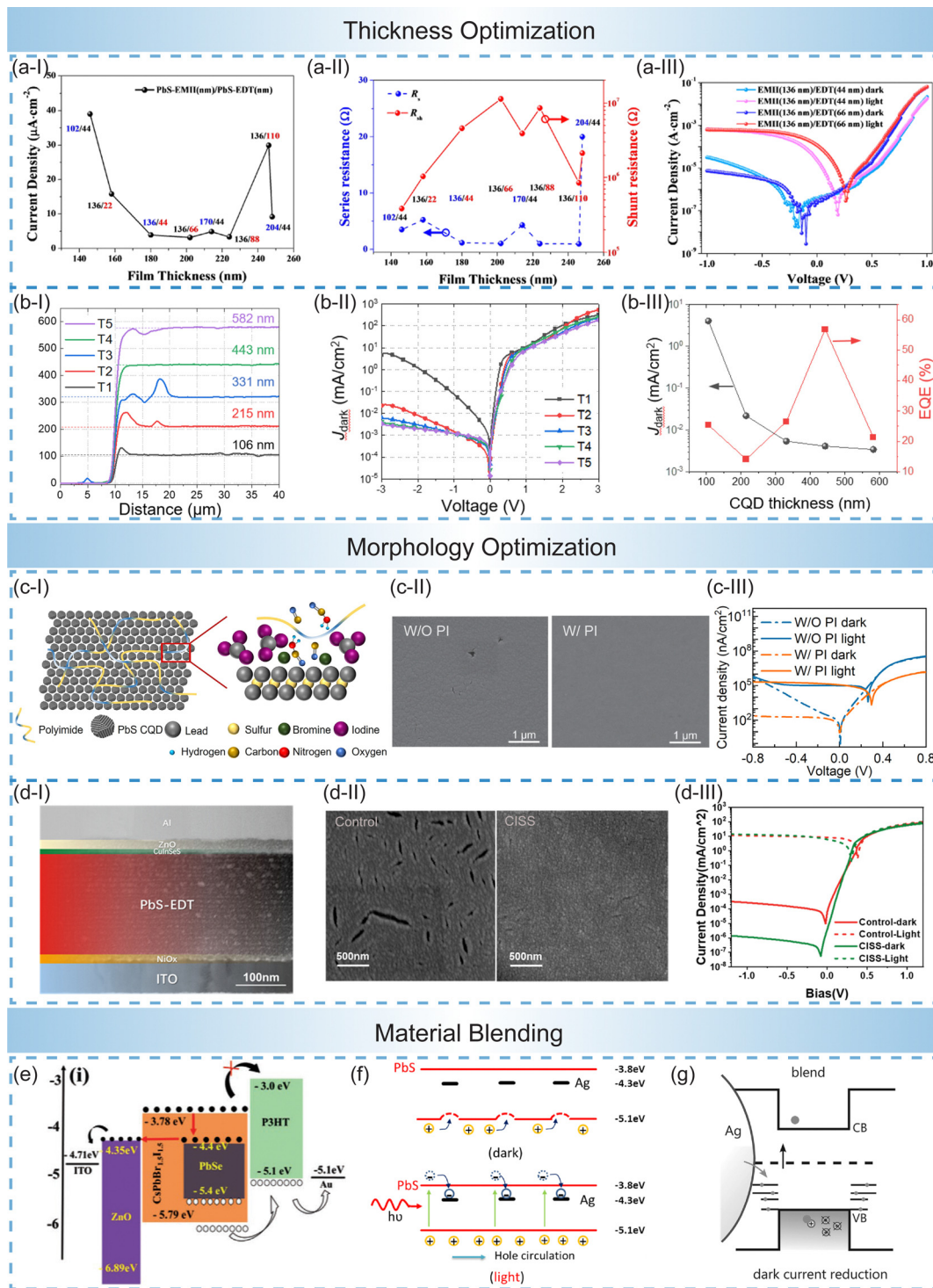


Fig. 15 Thickness, morphology and composition optimization of PbS CQDs films to suppress J_d . (a-I) Dependence of J_d and (a-II) Dependence of serial and shunt resistance on PbS CQDs film thickness. (a-III) $J-V$ curves of the PbS-EMII/PbS-EDT 136/44 nm and 136/66 nm devices in dark and under illumination. (b-I) The surface profile curves and (b-II) J_d-V curves of photodiodes utilizing different PbS CQDs film thicknesses. (b-III) Dependence of J_d and EQE on PbS CQDs film thickness. (c-I) Schematics of the PbS CQDs/PI composite films. (c-II) SEM images of the PbS CQDs films w/o and w/ PI. (c-III) $J-V$ curves of PbS CQDs photodiodes w/o and w/ PI in dark and under illumination. (d-I) Cross-sectional SEM images of PbS CQDs photodiode. (d-II) SEM images of PbS and PbS/CuInSeS CQDs films. (d-III) J_d-V curves of PbS CQDs photodiodes w/o and w/ CuInSeS layer. (e) Energy band diagram of electron transport in the PbSe-perovskite blending layer. (f) Schematics of local band bending and hole transport hindering caused by Ag nanocrystals. (g) Schematic of majority carrier reduction by Ag NPs doping. Figure reproduced with permission from: (a) ref. 50, [American Chemical Society], copyright [2022]; (b) ref. 51, [American Institute of Physics], copyright [2024]; (c) ref. 52, [Elsevier], copyright [2023]; (d) ref. 13, [Royal Society of Chemistry], copyright [2024]; (e) ref. 153, [John Wiley and Sons], copyright [2022]; (f) ref. 154, [American Chemical Society], copyright [2014]; (g) ref. 155, [John Wiley and Sons], copyright [2015].

reduced by an order of magnitude compared to a device with a PbS-EMII layer thickness of 102 nm. They explained that the thickness of the CQDs layer affects not only the densities of bulk and interface traps but also the shunt resistance (R_{sh}) (Fig. 15a-II). They observed that the trend of R_{sh} with thickness variation was opposite to the dependence of J_d on the active layer thickness of the CQDs. Since the shunt current, caused by R_{sh} , is a significant component of the dark current, fine-tuning of the thickness within a specific range is essential for achieving optimal performance. In addition, the thickness of PbS-EDT can also contribute to R_{sh} , trap states and thus J_d , as shown in Fig. 15a-III. Another study discovered that for devices with an Al/TiO₂/PbS-ZnI₂/NiO_x/ITO structure, when the active layer thickness exceeds 200 nm, the J_d under a reverse bias of -3 V rapidly decreases from 4.08 mA cm^{-2} to 3.4 A cm^{-2} (Fig. 15b).⁵¹ The authors attributed this reduction to the suppression of BTBT and the dominance of TAT arising from the increased depletion width in devices with thicker CQD layers, despite the negligible increase in serial resistance with thicker CQD layers.⁵¹ However, the impact of CQDs layer thickness on dark current is also influenced by device structure and fabrication processes. Therefore, further research is necessary to explore these correlations more precisely.

5.2.2 Morphology control. Improving the uniformity and quality of thin films in CQDs devices is a critical strategy for reducing device leakage current and dark current. During the preparation of CQDs thin films, ligands are typically mixed in a non-solvent for the ligand exchange process to replace insulating long-chain ligands with conductive short-chain ligands. The film is then immersed and rinsed to remove unreacted and exchanged ligands. For deposition of thick CQD films, this process utilizing a high-concentration CQD precursor in one step can lead to a significant volume reduction and the formation of cracks and voids in the film, thereby increasing leakage and dark currents and adversely affecting the device's detectivity. To mitigate these detrimental effects, films are usually fabricated using a layer-by-layer method that involves repeated CQDs deposition, ligand treatment, and washing steps, which enhances the film quality.¹⁵²

However, though such method could enhance film quality, it is time-consuming and incompatible with industrial-scale production, where it is generally preferable to fabricate the CQDs film layer by one-step spin-coating process directly from a high-concentration CQD ink. Liang *et al.* introduced a Lewis base polyimide (PI) into the CQDs ink, and the schematic of PbS CQDs/PI composite is shown in Fig. 15c-I.⁵² After introducing PI into the PbS CQDs ink, the monodispersity is significantly improved, resulting in improved defect passivation and film morphology of PbS CQDs (Fig. 15c-II). The resulting CQDs photodiodes showed a tenfold reduction in defect density and a two-order magnitude reduction in J_d at -0.4 V compared to control devices (Fig. 15c-III). In addition to improving the quality of the CQDs ink, the interface between the CQDs layer and the carrier transport layer is crucial. A recently reported low dark current (about 70 nA cm^{-2}) is attributed to a high-quality n-type CQDs solid film created *via* a novel solution-phase

ligand exchange method. This approach, combined with mild MA ligand passivation, results in an optimal surface chemical environment, effectively passivating top interface defects, and reducing recombination at the CQDs ink/HTL heterojunction interface.⁴⁷

Additionally, traditional SSLE techniques often cause inherent cracks, leading to significant leakage currents and limiting the sensitivity of detectors. To address this, Chen *et al.* introduced a CuInSeS CQDs interfacial layer on top of the PbS-EDT CQDs layer, and the device schematic is shown in Fig. 15d-I.¹³ After the modification of interfacial CuInSeS layer, the CQDs active layer results in a smoother and crack-free layer (Fig. 15d-II), which is expected to improve the interfacial contact between PbS CQDs and ZnO films. Benefiting from the improved film morphology and band alignment, J_d is significantly suppressed from $2 \times 10^{-7}\text{ A cm}^{-2}$ to $1.15 \times 10^{-9}\text{ A cm}^{-2}$ under -1 V bias (Fig. 15d-III).

5.2.3 Material blending. In addition to improving film quality, Sulaman *et al.* proposed the integration of PbSe CQDs with inorganic mixed halide perovskite nanomaterials to fabricate high-performance photodetectors based on bulk heterojunctions (BHJ) (Fig. 15e).¹⁵³ By physically blending PbSe CQDs with fully inorganic mixed halide perovskite nanocrystals, specifically PbS_{0.5}I_{1.5}, partial donor-acceptor interpenetration occurs, forming a pristine phase. This configuration reduces carrier transport in the dark state and enhances photocurrent under illumination, achieving a D^* of $5.96 \times 10^{13}\text{ Jones}$.

Furthermore, under high-temperature and strong electric field conditions, halide ion migration through vacancies can increase defect density in the CQDs layer and block device interfaces, resulting in an increased J_d and delayed saturation voltage. Chen *et al.* introduced polyimide (PI) into CQDs films to effectively block halide ion migration,¹⁴⁶ thereby reducing J_d under high bias and enhancing the stability of CQDs photodiodes under high-temperature and strong electric fields.

The dark current characteristics of photodetectors can also be optimized through plasmonic structures. He *et al.* demonstrated that co-depositing Ag nanoparticles (NPs) into the CQDs solution reduces device dark current. In darkness, Ag NPs induce local band bending and hinder hole transport, thus reducing dark current (Fig. 15f).¹⁵⁴ A significant reduction in dark currents, up to two orders of magnitude, has been reported in ligand-exchanged PbS-based photodetector devices when PbS NPs are blended with 10% Ag nanocrystals (NCs).¹⁵⁵ The Ag NCs, acting as electron donors due to their low work function, can effectively passivate the shallow electron traps present in the bandgap, thereby reducing the concentration of majority holes in the PbS films (Fig. 15g).

5.2.4 Trap states management. CQDs have a high surface-to-volume ratio, making them particularly susceptible to defect-induced recombination of excited states. These trap states are traditionally attributed to dangling bonds formed by surface discontinuities in the crystal structure. PbX typically occupy the intermediate space in the near-infrared spectrum and have become the mainstream choice for SWIR detector applications in recent years. Compared to many III-V CQDs, the synthesis of

high-quality PbX CQDs is relatively straightforward and can be achieved using simple methods such as hot-injection techniques. The synthesized CQDs are typically covered with long aliphatic chains to enhance their colloidal stability. However, most applications require casting these CQDs into films and improving carrier mobility. Therefore, shorter entities are often used to replace the long insulating ligands like OA. Moreover, selecting appropriate strong coordinating ligands is crucial for enhancing film stability and reducing the density of defect sites. For instance, passivating the interface and bulk defects with PbI_2 can reduce J_d to less than one-tenth of that in control devices.¹⁵⁶ Studies have shown that the crystallographic facet exposed by PbS CQDs significantly impacts the presence of surface defects. As the CQDs size increases, PbX CQDs transform from octahedra terminated with (111) facets to truncated octahedra with more additional (100) facets. Specifically, PbS(111) facets are terminated with either sulfur or lead atoms, while (100) facets have both sulfur and lead terminations. Due to the electroneutrality, the (100) facets are challenging to be passivated by ligands, resulting in the formation of dangling bonds. These unpassivated sites are a significant source of deep-level traps and the nonuniformity of the films. Liu *et al.* addressed passivation of (100) facets in large-size CQDs by introducing a bidentate ligand of 4-(aminomethyl)pyridine (4-AMPY) with a high absorption energy on (100) facets to complement halide termination (Fig. 16a-I),⁵³ thereby suppressing tail states and reducing defect concentration. Both ends of 4-AMPY exhibit similar bonding capabilities on (100) facets, suggesting effective co-passivation with Br (Fig. 16a-II). This strategy achieved a highly suppressed J_d of 9.6 nA cm^{-2} at -10 mV (Fig. 16a-III).

Notably, the amount of surface ligands in the solution has also been reported to induce atomic rearrangement, thereby altering the shape of CQDs and contributing to the passivation of the defect site. Vafaie *et al.* pursued a novel approach to obtain high-quality films for large-size PbS CQDs ($> 5 \text{ nm}$).⁵⁴ Compared to low-level bromine (LLB) treatment, high-level bromine (HLB) treatment ($2:5 \text{ PbBr}_2/\text{PbI}_2$) effectively passivated the (100) and (111) facets and introduced dual-passivation to remove unwanted residual organics and enhance CQDs colloidal stability (Fig. 16b-I), resulting in a tenfold reduction in J_d compared to controlled photodiodes at -1 V (Fig. 16b-II). Similarly, Yang *et al.* developed an excess concentration PbBr_2 ligand strategy for large-size PbS CQDs to effectively suppress the defects and increase the carrier lifetime,⁵⁵ resulting in a minimal J_d of 156 nA cm^{-2} at -0.1 V (Fig. 16c).

In recent years, the approach of passivating surface defects in PbS CQDs by introducing perovskite materials has garnered significant attention due to its potential to markedly enhance their optoelectronic performance. Chen *et al.* proposed a novel passivation strategy for large-size ($d > 4 \text{ nm}$) PbS CQDs using halide perovskite $\text{CsPbI}_{3-x}\text{Br}_x$ heteroepitaxial bridging of charge-neutral (100) facets by adding a small amount of CsI in the PbX_2 ligand solution.⁵⁶ This approach led to reduced defect states and improved dispersion stability (Fig. 16d-I&II), yielding perofilms with enhanced EQE, decreased J_d from

$1 \times 10^{-6} \text{ A cm}^{-2}$ to $2 \times 10^{-7} \text{ A cm}^{-2}$ at -0.4 V (Fig. 16d-III), and increased operational stability compared to control CQDs photodiodes. Similarly, a high-performance PbS CQDs based broadband photodetector incorporates small molecular-scaled (1 nm) $\text{CH}_3\text{NH}_3\text{PbI}_3$ perovskite hybrids that function both as trap state passivators and visible light sensitizers.¹⁵⁷ This integration reduces J_d from $9.4 \times 10^{-8} \text{ A cm}^{-2}$ to $2.1 \times 10^{-9} \text{ A cm}^{-2}$ at 0 bias, effectively minimizing the recombination losses and enhancing the broadband photoresponse. Furthermore, the surface morphology and chemical state of PbS CQDs significantly influence perovskite crystallization. Therefore, selecting appropriate halide ligands is crucial for achieving PbS CQDs with high conductivity, good morphology, suitable surface chemical states, and compatible energy levels with perovskites. The impact of different ligands on dark current can also vary by up to two orders of magnitude.¹⁵⁸ However, the effect of different ligands on photocurrent should also be considered to achieve high detectivity.

For other photomaterials like HgTe CQDs, Ackerman *et al.* optimized HgTe CQDs/ Ag_2Te CQDs photodiodes in the SWIR range by introducing HgCl_2 in the EDT/hydrochloric acid (HCl) exchange process,¹⁵⁹ significantly enhancing R_{sh} and reducing J_d by tenfold at -500 mV reverse bias from approximately $4 \times 10^{-3} \text{ A cm}^{-2}$ to $4 \times 10^{-4} \text{ A cm}^{-2}$. Through their discussions, it was determined that the majority of the improvements stemmed from a reduction in non-radiative recombination rather than solely from a decrease in mobility. Additionally, Yu *et al.* employed precursor reactivity engineering, using an Se stabilization strategy based on HgTe CQDs surface Se coating (Fig. 16e-I).⁵⁷ This can significantly improve the colloidal dispersion of CQDs ink (Fig. 16e-II), along with improved defect passivation and doping modulation. The resulting Se:HgTe CQDs SWIR photodetector exhibits an ultra-low J_d of $3.26 \times 10^{-6} \text{ A cm}^{-2}$ at -0.4 V , which is significantly reduced by an order of magnitude compared to the control HgTe CQDs devices (Fig. 16e-III). Yang *et al.* also fabricated a PIN photodiode using thermally evaporated Bi_2Se_3 film/HgTe CQDs/ Ag_2Te CQDs stacking technology.¹⁶⁰ This device employed a ligand engineering approach to produce well-separated HgTe CQDs with a sharp absorption edge, achieving a rectification ratio of two thousand and a J_d of $2.3 \times 10^{-6} \text{ A cm}^{-2}$ under -0.4 V reverse bias.

For CuInSe_2 CQDs devices, Guo *et al.* demonstrated that Mn^{2+} doping improves CuInSe_2 CQDs crystal quality.¹⁶¹ The Mn^{2+} doping acts as a hole capturer forming charge compensating pairs with Cu^{2+} defects, leading to long-lived Cu^{2+} radiative recombination. Furthermore, Mn^{2+} doping alters the conduction band minimum and valence band maximum levels, enhancing carrier transport properties. The optimal Mn^{2+} doping level (0.01 Mn feed ratio) balanced these factors, achieving a suppressed J_d of $1.6 \times 10^{-10} \text{ A cm}^{-2}$.

Finally, Table 1 contains a summary of representative strategies to suppress J_d of CQDs photodiodes published recently. In each work, the main J_d mechanisms, experimental approach to suppress J_d and resulting photodetection performance including detection wavelength, J_d , R and D^* are provided.

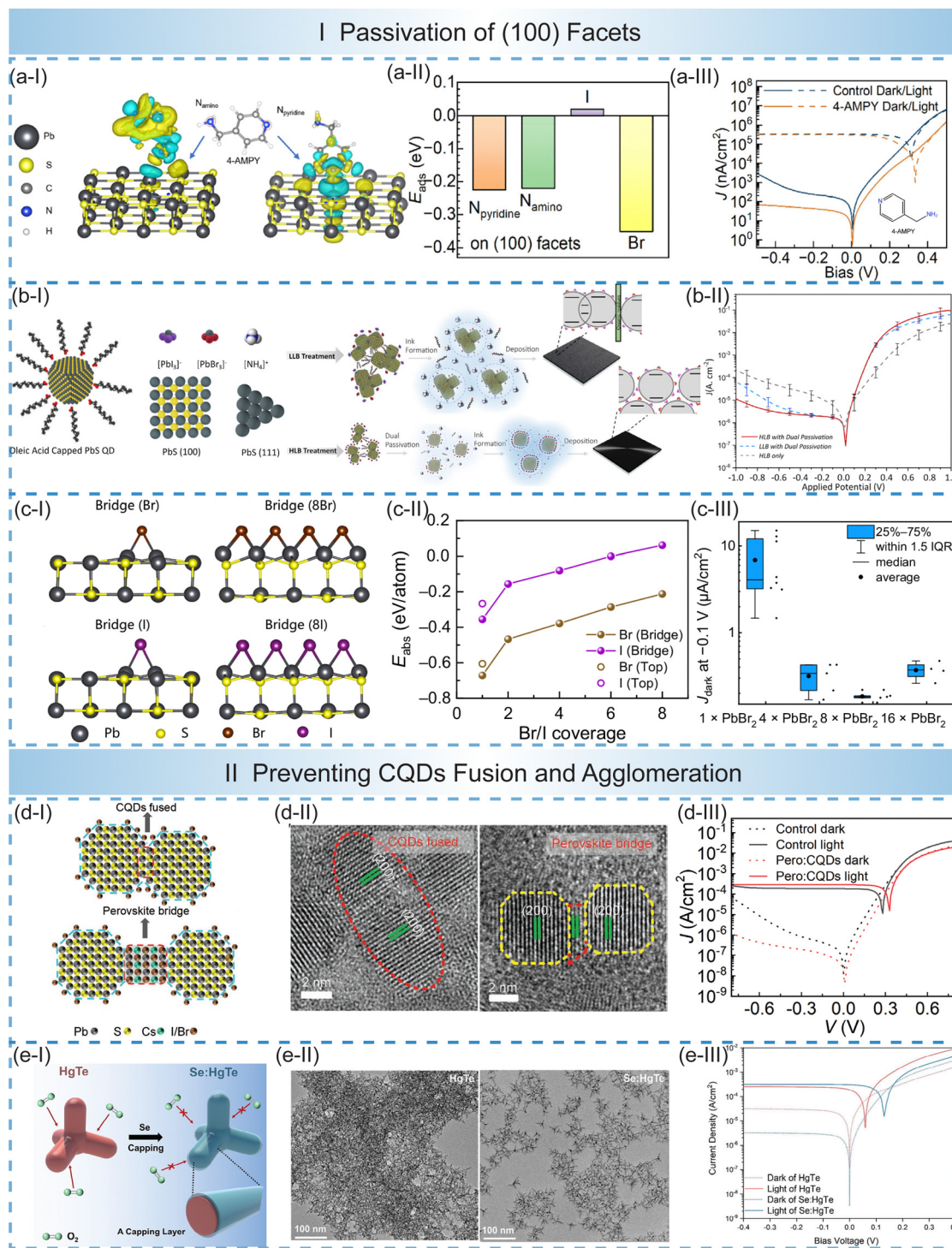


Fig. 16 Trap state management in PbS CQDs films to suppress J_d . (a-I) Differential charge densities of 4-AMPY adsorption on the (001) facet of PbS CQDs. (a-II) Adsorption energies of N_{amino} , $\text{N}_{\text{pyridine}}$, I^- and Br^- on PbS(100) facet. (a-III) J – V curves of PbS CQDs photodiodes w/o and w/4-AMPY passivation in dark and under 1300 nm illumination. (b-I) Schematic diagram of low level of lead bromide (LLB) and high level of lead bromide (HLB) treatment methods. (b-II) J_d – V curves of devices with different exchange routes versus control ones. (c-I) Diagrams of PbS CQDs (100) facets passivated by 1Br^- , 1I^- , 8Br^- , and 8I^- . (c-II) Adsorption energy versus Br/I coverage curves. (c-III) J_d of devices passivated by increasing concentrations of PbBr_2 at -0.1 V . (d-I) Schematic diagram and (d-II) TEM images of the fused and perovskite-bridged CQDs. (d-III) J – V curves of control and perovskite-bridged PbS CQDs photodiodes in dark and under 1300 nm illumination. (e-I) Schematic of Se:HgTe and HgTe CQDs and their abilities against oxidation. (e-II) TEM images of HgTe and Se:HgTe CQDs. (e-III) J – V curves of HgTe and Se:HgTe CQDs photodiodes in dark and under 1550 nm illumination. Figure reproduced with permission from: (a) ref. 53, [John Wiley and Sons], copyright [2024]; (b) ref. 54, [Elsevier], copyright [2021]; (c) ref. 55, [American Physical Society], copyright [2023]; (d) ref. 56, [John Wiley and Sons], copyright [2023]; (e) ref. 57, [John Wiley and Sons], copyright [2024].

Table 1 Overview of representative J_d mechanisms, experimental suppression approaches and photodetection performances in CQDs SWIR photodiodes at room temperature

Device structure	λ_{peak} (nm)	J_d mechanism	J_d reduction strategies	J_d (A cm^{-2})	R (A W^{-1})	D^* (fones) ¹	Ref.
ITO/Pbs-EDT/Pbs-mixed halide/Pbs-TFCA/Ag	1450	Reverse injection	Strong ligand passivation of HBL	1×10^{-6} @-1 V	0.766@-1 V	3×10^{10} @0 V@10 kHz	37
ITO/SnO _x /C ₆₀ /Pbs/NiO/Au	1550	Reverse injection	Heterojunction interface modification of HBL	1×10^{-7} @-10 mV	0.82@-10 mV	6.67×10^{11} @-10 mV@100 kHz	38
ITO/ZnO/Pbs/Pbs-EDT/Au	950	Reverse injection	ALD ZnO reducing oxygen adsorption	2.9×10^{-8} @-1 V	0.536@-1 V	1.66×10^{11} @-1 V@10 kHz	39
ITO/ZnO/Pbs-BTA/Pbs-EDT/Au	1300	Reverse injection	[002]-oriented ZnO reducing H ₂ O absorption	8.49×10^{-8} @-0.1 V	0.552@-0.1 V	2.15×10^{12} @0 V@94.6 kHz	40
ITO/NiO/Pbs-BDT/ZnO/AI	1135	Reverse injection	Energy level blocking	3.4×10^{-8} @-1 V	0.2@-1 V	1.1×10^{12} @-1 V@100 Hz	41
ITO/ZnO/Pbs-I&Br/Pbs-EDT/Au	1300	Reverse injection	Passivation of interface defects by oxidation control	2.18×10^{-7} @-0.6 V	0.33@0 V	6.8×10^{12} @0 V@45 kHz	42
ITO/MoO ₃ /FTB/PbsSe/ZnO/Al	1100	Reverse injection	Energy level blocking	2×10^{-7} @-1 V	0.05@-1 V	3×10^{11} @-0.5 V ^a	43
FTO/TiO ₂ /Pbs-QDs/CuSCN/Au	1258	Reverse injection	Energy level blocking	6×10^{-9} @-1 V	0.2@-1 V	7×10^{10} @-1 V ^a	44
ITO/PEDOT:PSS/PbSe/ZnO/ Poly-TPD/PbSe/ZnO/Al	1100	Reverse injection	Coupling of double active layer	4×10^{-7} @-0.5 V	0.14@-0.5 V	1×10^{12} @-0.5 V ^a	45
FTO/SnO _x /Hg ₂ Te/Ag ₂ Te/Au	1750	Reverse injection	Energy level blocking	2×10^{-5} @-0.2 V	0.3@0 V	5×10^{10} @0 V@1 kHz	46
ITO/LiF/SnO _x /Pbs-I/ Pbs-MAMoO _x /Au	1050	Reverse injection	Carrier-selective layer at HTL/electrode interface	7×10^{-8} @-0.5 V	0.61@-0.5 V	1.42×10^{12} @-0.5 V@100 Hz	47
ITO/ZnO/Pbs-I&Br/Pbs-EDT/Au	1290	Reverse injection (trap-assisted)	SIL passivation layer at HTL/electrode interface	5.94×10^{-7} @-0.05 V	0.48@0 V	4.8×10^{12} @0 V@43 kHz	48
ITO/NiO _x /Pbs/ZnO/Al	1390	Reverse injection (trap-assisted)	Surface Passivation of HTL at HTL/electrode interface	1.58×10^{-7} @-0.5 V	0.62@-0.5 V	2.05×10^{12} @-0.5 V@1 kHz	49
Au/Pbs-EDT/Pbs-EMII/SnO _x /ITO	1100	TAT & shunt & reverse injection	Optimization of CQDs thickness	3.15×10^{-6} @-0.5 V	0.24@-0.5 V	1.24×10^{10} @-0.5 V@100 Hz	50
Al/TiO ₂ /Pbs-ZnI ₂ :MPA/NiO _x /ITO	1420	TAT & shunt	Optimization of CQDs thickness	4.1×10^{-6} @-3 V	0.65@-3 V	1.78×10^{12} @-3 V ^a	51
Au/Pbs-EDT/Pbs-PbX ₂ /ZnO/I _{TO}	1300	TAT & shunt	PI passivating Pb ₃ -PbX ₂ interface defects	1.23×10^{-9} @-0.1 V	0.36@0 V	6.36×10^{12} @0 V@100 kHz	52
ITO/NiO _x /Pbs-EDT/CuInSe/ZnO/Al	940	TAT & shunt	Introducing CuInSe CQDs interfacial layer	1×10^{-9} @-1 V	0.23@-1 V	1.87×10^{12} @-1 V ^a	13
Au/Pbs-EDT/Pbs-4-AMPY/ZnO/I _{TO}	1300	SRH & TAT	Supplemental double-ended ligands exchange	7×10^{-8} @-0.5 V	0.532@-0.5 V	2.5×10^{12} @-0.5 V@100 kHz	53
Au/Pbs-EDT/Pbs-PbX ₂ /ZnO/I _{TO}	1550	SRH & TAT	Introducing an added exchange step	1.6×10^{-6} @-0.1 V	1@0 V	8×10^{11} @0 V@500 kHz	54
Au/Pbs-EDT/Pbs-&Br/ZnO/I _{TO}	1300	TAT	Excessive PbBi ₂ concentration	1.8×10^{-7} @-0.1 V	0.239@-0.1 V	5.22×10^{12} @0 V@38 kHz	55
Au/Pbs-EDT/Pbs-Pero/ZnO/I _{TO} /Au	1300	SRH & TAT	ligand exchange strategy	9×10^{-8} @-0.1 V	0.54@0 V	6.2×10^{12} @0 V@42 kHz	56
Au/Se:HgTe/Bi ₂ S ₃ /ITO	2000	SRH & TAT	(100) facets epitaxially bridged with perovskite Surface coating of Se on HgTe CQDs	2.7×10^{-6} @-0.1 V	0.69@0 V	5.17×10^{11} @0 V@500 Hz	57

^a The values not annotated with @Hz were calculated considering only shot noise, with other noise sources disregarded.

6. Conclusions

In summary, CQDs SWIR photodiodes offer significant advantages over conventional III-V binary and ternary semiconductor photodetectors including bandgap tunability over the entire SWIR region and ease of monolithic integration with Si ROICs *via* solution processing, which potentially facilitate wide applications of CQDs SWIR imagers in machine vision, autonomous driving and augmented reality. Achievement in CQDs synthesis strategies and device fabrication techniques promote the rapid progress in SWIR photodetection performances, based on which semi-commercial prototyping image sensor chips have been implemented. For most applications, minimizing J_d is crucial to improve important figures of merit such as noise current, SNR, LDR and D^* . An overview of J_d values reported in recent years shows a large spread in J_d values, which deviate significantly from the calculated intrinsic limits of J_d . Based on theoretical and experimental analysis, we identified the dominant contribution mechanisms to J_d which include reverse injection from electrodes, diffusion and drift currents, SRH generation–recombination currents, trap-assisted tunneling, and shunt/leakage currents. Besides, the main affecting factors to J_d have been clearly pointed out, which include extrinsic (*e.g.*, energy level alignment, thickness and surface morphology, damage induced by specific fabrication procedures) and intrinsic (*e.g.*, trap state density in bulk and interfaces, energetic disorder of CQDs active layer) ones. Therefore, it is believed that once extrinsic contributions to J_d have been eliminated, J_d could be further reduced by minimizing the trap state density and energetic disorder in CQDs photodiodes.

While enormous progress has been made in origins and suppression of J_d in CQDs SWIR photodiodes, more attention needs to be paid to further minimize J_d while retaining EQE, as shown in the following aspects.

Firstly, a quantitatively physical model of J_d should be established for understanding CQDs device characteristics both in dark and under illumination. The current experimental research predominantly employs the popular Shockley–Quiesser (S–Q) diode model, based on which the main components for J_d were obtained by curve fitting of the measured J_d versus V curves. However, the S–Q diode model does not capture the underlying physics of CQDs junctions. In 2023, Arya *et al.* developed a compact and easy-to-use physical model for CQDs junctions assuming that the transport of carriers across the CQDs layer obeys the thermionic emission and tunneling processes.¹⁶² However, the surface state and size non-uniformity among CQDs, assembly and energetic disorder in CQDs films and high density of trap states is negligible in this model, which are main factors affecting the charge transport behaviors as discussed above and should be taken into account in the modeling of CQDs photodiodes. Moreover, owing to structural and energetic disorder in the CQDs assembly, hopping model is usually adopted for characterization of charge transport behaviors of solution-processed CQDs, and thus we should consider the establishment of device model based on hopping mechanisms in future studies.

Secondly, as discussed above, trap states both in bulk and at interfaces contribute significantly to carrier trapping/detrapping process and thus high J_d in CQDs SWIR photodiodes, and thus various defect passivation strategies have been developed to effectively suppress J_d . However, it still remains unclear which kinds of trap states are dominant factors responsible for J_d , and thus advanced defect characterization techniques including temperature-dependent low-frequency noise spectra, temperature-dependent charge transport behaviors, photoluminescence spectroscopy, *etc.* should be employed to determine the main defect categories dominating J_d . Herein, the size dependence should be considered. Moreover, except for deep-level mid-gap states coming from physical defects at the CQDs surface, surface –OH groups have been experimentally confirmed to trigger the epitaxial CQDs fusion/dimerization. Several experimental reports have attributed carrier trapping to the –OH groups and CQDs fusion in CQDs solar cells, whereas the effects of such trap states on J_d is so far lacking. Furthermore, the shift of entire electronic band structure induced by reduction (oxidation) of p-type (n-type) doped CQDs usually results in a hole (or electron) trap, hindering the construction of ideal PIN structure photodiodes. Therefore, passivation of physical defects at the CQDs surface, suppression of dimerization or fusion and challenges for efficient doping of CQDs, while maintaining trap-free conduction, were identified as key strategies to minimize J_d . Future device research will aim at employing this insight from aspects of defect physics and passivation strategies to further reduce J_d .

Thirdly, the mainstream device structure for reported CQDs photodiodes is PIN diode structure, where CQDs active layer is employed as intrinsic layer to combine with p-n-type carrier transport/blocking layer. The reported PIN structured CQDs photodiodes are mainly concentrated on the 1–2 μm detection range. However, when the detection range exceeds 2 μm , the bandgap of CQDs decreases with gradual change of conduction and valence band levels. It is thus challenging for the energy level alignment between small-bandgap CQDs and carrier transport layer, posing significant difficulty in obtaining a rather low J_d level in PIN photodiodes. Future research could focus on modulating the energy level and carrier concentration of carrier transport layers by doping and CQDs by surface state modification. Moreover, novel device structures such as barrier-type, quantum-tuned cascade multijunction, *etc.* could be an alternative to obtain low dark current and high photoresponse in CQDs photodiodes with a detection range higher than 2 μm .

Finally, more attention should be paid to device performances after long-term bias and illumination stress. In practical applications, long-term reverse bias and light illumination stress is usually applied to the device, and how the device performances especially J_d and J_{ph} evolute after long-time large reverse bias and high light illumination requires to be systematically investigated. Moreover, after fabrication of CQDs SWIR photodiodes, the wafer should further undergo the back end of line (BEOL) process, which is mainly composed of interconnection between top electrodes of photodiodes and ROICs, deposition of passivation layer and final wafer level packaging. In the

BEOL process, the effects of annealing at an evaluated temperature, temperature cycling, exposure to various gases and chemicals and deposition of light management layer and transparent passivation layer onto the device stack remains unclear, and need to be further explored in detail. This is critical for fabricating high-performance CQDs SWIR image sensor wafers and their practical applications.

Data availability

No primary research results, software or code have been included and no new data were generated or analysed as part of this review.

Conflicts of interest

The authors declare no conflict of interest.

Acknowledgements

This work was supported by the Project on Frontier and Interdisciplinary Research Assessment, Academic Divisions of the Chinese Academy of Sciences (Grant No. XK2023XXA002), the National Natural Science Foundation of China (Grant No. 62374110), National Key Research and Development Program of China (No. 2023YFD1702600, 2022YFB3205503), the Shenzhen Science and Technology Program (Grant No. JCYJ20230808105806014), State Key Laboratory of Radio Frequency Heterogeneous Integration (Independent Scientific Research Program No. 2024014 and Open Scientific Research Program No. KF2024007), and Collaborative Innovation Centre of Suzhou Nano Science and Technology.

References

- X. Guan, X. Yu, D. Periyangounder, M. R. Benzigar, J.-K. Huang, C.-H. Lin, J. Kim, S. Singh, L. Hu, G. Liu, D. Li, J.-H. He, F. Yan, Q. Wang and T. Wu, *Adv. Opt. Mater.*, 2020, **9**, 2001708.
- Z. Wu, Y. Zhai, H. Kim, J. D. Azoulay and T. N. Ng, *Acc. Chem. Res.*, 2018, **51**, 314.
- M. Razeghi, A. Haddadi, X. Suo, S. Adhikary, P. Dianat, R. Chevallier, A. Hoang and A. Dehzangi, *Infrared Technology and Applications XLII*, 2016, p. 64.
- M. R. Atalla, Y. Kim, S. Assali, D. Burt, D. Nam and O. Moutanabbir, *ACS Photonics*, 2023, **10**, 1649.
- S. Sarkar, P. Le, J. Geng, Y. Liu, Z. Han, M. U. Zahid, D. Nall, Y. Youn, P. R. Selvin and A. M. Smith, *J. Am. Chem. Soc.*, 2020, **142**, 3449.
- C. Livanelioglu, Y. Ozer and S. Kocaman, *J. Opt. Soc. Am. B*, 2020, **37**, 56.
- S. Bianconi and H. Mohseni, *Rep. Prog. Phys.*, 2020, **83**, 044101.
- Y. Shi, Z. Wu, X. Dong, P. Chen, J. Wang, J. Yang, Z. Xiang, M. Shen, Y. Zhuang, J. Gou, J. Wang and Y. Jiang, *Nanoscale*, 2021, **13**, 12306.
- E. H. Sargent, *Adv. Mater.*, 2008, **20**, 3958.
- M. S. Pavlović, P. D. Milanović, M. S. Stanković, D. B. Perić, I. V. Popadić and M. V. Perić, *Sensors*, 2022, **22**, 2562.
- P. Wang, H. Xia, Q. Li, F. Wang, L. Zhang, T. Li, P. Martyniuk, A. Rogalski and W. Hu, *Small*, 2019, **15**, 1904396.
- C. Xie, J. Xu, Y. Wang, W. Yang, Y. Zhao, S. Wang, H. Liu, Q. Wang, X. Yuan, W. Zeng and Z. Huang, *IEEE Trans. Electron Dev.*, 2022, **69**, 6201.
- Z. Chen, T. Huang, B. Zhang, C. Wu, X. Zhang, T. Sun, W. Xu, K. Kang, C. Xiang, T. Zhang and R. Li, *J. Mater. Chem. C*, 2024, **12**, 4493.
- B. K. Jung, H. K. Woo, C. Shin, T. Park, N. Li, K. J. Lee, W. Kim, J. H. Bae, J.-P. Ahn, T. N. Ng and S. J. Oh, *Adv. Opt. Mater.*, 2022, **10**, 2101611.
- Y. Liu, J. Liu, C. Deng, B. Wang, B. Xia, X. Liang, Y. Yang, S. Li, X. Wang, L. Li, X. Lan, P. Fei, J. Zhang, L. Gao and J. Tang, *Adv. Mater.*, 2024, 2313811.
- P. E. Malinowski, V. Pejović, E. Georgitzikis, J. H. Kim, I. Lieberman, N. Papadopoulos, M. J. Lim, L. M. Hagelsieb, N. Chandrasekaran, R. Puybaret, Y. Li, T. Verschooten, S. Thijs, D. Cheyns, P. Heremans and J. Lee, 2022 International Electron Devices Meeting (IEDM), 2022, p. 19.3.1.
- A. Rogalski, *Opto-Electron. Rev.*, 2012, **20**, 279.
- S. Zhang, C. Bi, T. Qin, Y. Liu, J. Cao, J. Song, Y. Huo, M. Chen, Q. Hao and X. Tang, *ACS Photonics*, 2023, **10**, 673.
- V. Pejović, J. Lee, E. Georgitzikis, Y. Li, J. H. Kim, I. Lieberman, P. E. Malinowski, P. Heremans and D. Cheyns, *IEEE Electron Dev. Lett.*, 2021, **42**, 1196.
- X. Li, J. Zhang, C. Yue, X. Tang, Z. Gao, Y. Jiang, C. Du, Z. Deng, H. Jia, W. Wang and H. Chen, *Sci. Rep.*, 2022, **12**, 7681.
- I. Shafir, N. Snapi, D. Cohen-Elias, A. Glozman, O. Klin, E. Weiss, O. Westreich, N. Sicron and M. Katz, *Appl. Phys. Lett.*, 2021, **118**, 063503.
- R. Kumar, D. Panda, J. Saha, S. A. Gazi and S. Chakrabarti, *Superlattices Microstruct.*, 2020, **148**, 106714.
- A. Rogalski, P. Martyniuk, M. Kopytko, P. Madejczyk and S. Krishna, *Sensors*, 2020, **20**, 7047.
- C. Livanelioglu, Y. Ozer and S. Kocaman, *J. Opt. Soc. Am. B*, 2020, **37**, 56.
- S. Bianconi and H. Mohseni, *Rep. Prog. Phys.*, 2020, **83**, 044101.
- S. Bao, Y. Wang, K. Lina, L. Zhang, B. Wang, W. A. Sasangka, K. E. K. Lee, S. J. Chua, J. Michel and E. Fitzgerald, *J. Semicond.*, 2021, **42**, 023106.
- M. R. Atalla, S. Assali, S. Koelling, A. Attiaoui and O. Moutanabbir, *ACS Photonics*, 2022, **9**, 1425.
- O. Moutanabbir, S. Assali, X. Gong, E. O'Reilly, C. A. Broderick, B. Marzban, J. Witzenz, W. Du, S.-Q. Yu, A. Chelnokov, D. Buca and D. Nam, *Appl. Phys. Lett.*, 2021, **118**, 110502.
- H. Tran, T. Pham, J. Margetis, Y. Zhou, W. Dou, P. C. Grant, J. M. Grant, S. Al-Kabi, G. Sun, R. A. Soref, J. Tolle,

- Y.-H. Zhang, W. Du, B. Li, M. Mortazavi and S.-Q. Yu, *ACS Photonics*, 2019, **6**, 2807.
- 30 F. Cao and L. Li, *Adv. Funct. Mater.*, 2021, **31**, 2008275.
- 31 M. Peng, Y. Liu, F. Li, X. Hong, Y. Liu, Z. Wen, Z. Liu, W. Ma and X. Sun, *ACS Appl. Mater. Interfaces*, 2021, **13**, 51198.
- 32 I. Ramiro, O. Özdemir, S. Christodoulou, S. Gupta, M. Dalmases, I. Torre and G. Konstantatos, *Nano Lett.*, 2020, **20**, 1003.
- 33 I. Ka, V. Le Borgne, K. Fujisawa, T. Hayashi, Y. A. Kim, M. Endo, D. Ma and M. A. El Khakani, *Mater. Today Energy*, 2020, **16**, 100378.
- 34 Y. M. Lee, J. H. Song, B. K. Jung, W. Kim, Y. K. Choi, J. Ahn, J. Park, J. Kwak and S. J. Oh, *Chem. Eng. J.*, 2024, **488**, 150916.
- 35 L. Gao, L. Wang, A. V. Kuklin, J. Gao, S. Yin, H. Ågren and H. Zhang, *Small*, 2021, **17**, 2105683.
- 36 J. S. Steckel, E. Josse, A. G. Pattantyus-Abraham, M. Bidaud, B. Mortini, H. Bilgen, O. Arnaud, S. Allegret-Maret, F. Saguin, L. Mazet, S. Lhostis, T. Berger, K. Haxaire, L. L. Chapelon, L. Parmigiani, P. Gouraud, M. Brihoum, P. Bar, M. Guillermot, S. Favreau, R. Duru, J. Fantuz, S. Ricq, D. Ney, I. Hammad, D. Roy, A. Arnaud, B. Vianne, G. Nayak, N. Virollet, V. Farys, P. Malinge, A. Tournier, F. Lalanne, A. Crocherie, J. Galvier, S. Rabary, O. Noblanc, H. Wehbe-Alause, S. Acharya, A. Singh, J. Meitzner, D. Aher, H. Yang, J. Romero, B. Chen, C. Hsu, K. C. Cheng, Y. Chang, M. Sarmiento, C. Grange, E. Mazaleyrat and K. Rochereau, 2021 IEEE International Electron Devices Meeting (IEDM), 2021, p. 23.4.1.
- 37 Y. Zhang, M. Vafaie, J. Xu, J. M. Pina, P. Xia, A. M. Najarian, O. Atan, M. Imran, K. Xie, S. Hoogland and E. H. Sargent, *Adv. Mater.*, 2022, **34**, 2206884.
- 38 L. Zhang, L. Chen, J. Yang, J. Liu, S. Lu, X. Liang, X. Zhao, Y. Yang, J. Hu, L. Hu, X. Lan, J. Zhang and L. Gao, *Nano Lett.*, 2023, **23**, 6489.
- 39 D. H. Parmar, J. M. Pina, T. Zhu, M. Vafaie, O. Atan, M. Biondi, A. M. Najjariyan, S. Hoogland and E. H. Sargent, *Adv. Mater.*, 2022, **34**, 2200321.
- 40 S. Lu, P. Liu, J. Yang, S. Liu, Y. Yang, L. Chen, J. Liu, Y. Liu, B. Wang, X. Lan, J. Zhang, L. Gao and J. Tang, *ACS Appl. Mater. Interfaces*, 2023, **15**, 12061.
- 41 J. R. Manders, T.-H. Lai, Y. An, W. Xu, J. Lee, D. Y. Kim, G. Bosman and F. So, *Adv. Funct. Mater.*, 2014, **24**, 7205.
- 42 Y. Wang, H. Hu, M. Yuan, H. Xia, X. Zhang, J. Liu, J. Yang, S. Xu, Z. Shi, J. He, J. Zhang, L. Gao, J. Tang and X. Lan, *ACS Appl. Mater. Interfaces*, 2023, **15**, 58573.
- 43 G. Sarasqueta, K. R. Choudhury, J. Subbiah and F. So, *Adv. Funct. Mater.*, 2011, **21**, 167.
- 44 I. Ka, L. F. Gerlein, I. M. Asuo, S. Bouzidi, D. M. Gedamu, A. Pignolet, F. Rosei, R. Nechache and S. G. Cloutier, *ACS Photonics*, 2020, **7**, 1628.
- 45 Z. Jiang, W. Hu, Y. Liu, W. Zhang, C. Mo, G. You, L. Wang, M. R. M. Atalla, Y. Zhang, J. Liu, K. K. Kurhade and J. Xu, *Appl. Phys. Lett.*, 2015, **107**, 091115.
- 46 C. Gréboval, E. Izquierdo, C. Abadie, A. Khalili, M. Cavallo, A. Chu, T. H. Dang, H. Zhang, X. Lafosse, M. Rosticher, X. Z. Xu, A. Descamps-Mandine, A. Ouerghi, M. G. Silly, S. Ithurria and E. Lhuillier, *ACS Appl. Nano Mater.*, 2022, **5**, 8602.
- 47 W. Gong, P. Wang, W. Deng, J. Li, W. Li, J. Li, Z. Chen, J. Li and Y. Zhang, *IEEE Trans. Electron Dev.*, 2023, **70**, 3668.
- 48 Y. Wang, H. Hu, X. Ran, L. Chen, M. Yu, P. Liu, J. He, J. Zhang, L. Gao, J. Tang and X. Lan, *ACS Photonics*, 2024, **11**, 1734.
- 49 Q. Yang, H.-W. Huang, G. Xu, Y. Yuan, M.-T. Jiang, Y.-N. Zhong, X. Gao, J.-L. Xu and S.-D. Wang, *Appl. Phys. Lett.*, 2023, **123**, 213302.
- 50 W. Gong, P. Wang, W. Deng, X. Zhang, B. An, J. Li, Z. Sun, D. Dai, Z. Liu, J. Li and Y. Zhang, *ACS Appl. Mater. Interfaces*, 2022, **14**, 25812.
- 51 G.-S. Choi, M. J. Lim, I. Sutcu, J. Yu, P. Malinowski, S. Y. Lee and I. Lieberman, *Appl. Phys. Lett.*, 2024, **124**, 121103.
- 52 X. Liang, Y. Liu, P. Liu, J. Yang, J. Liu, Y. Yang, B. Wang, J. Hu, L. Zhang, G. Yang, S. Lu, G. Liang, X. Lan, J. Zhang, L. Gao and J. Tang, *Sci. Bull.*, 2023, **68**, 698.
- 53 P. Liu, S. Lu, J. Liu, B. Xia, G. Yang, M. Ke, X. Zhao, J. Yang, Y. Liu, C. Ge, G. Liang, W. Chen, X. Lan, J. Zhang, L. Gao and J. Tang, *InfoMat*, 2024, **6**, e12497.
- 54 M. Vafaie, J. Z. Fan, A. M. Najarian, O. Ouellette, L. K. Sagar, K. Bertens, B. Sun, F. P. G. de Arquer and E. H. Sargent, *Matter*, 2021, **4**, 1042.
- 55 J. Yang, S. Lu, B. Xia, P. Liu, Y. Yang, Z. Xiao, J. Zhang, L. Gao and J. Tang, *Phys. Rev. Appl.*, 2023, **19**, 014021.
- 56 D. Chen, Y. Liu, B. Xia, L. Chen, Y. Yang, G. Yang, J. Liu, S. Lu, C. Ge, P. Liu, J. Yang, G. Liang, X. Lan, X. Zeng, L. Li, J. Zhang, Z. Xiao, L. Gao and J. Tang, *Adv. Funct. Mater.*, 2023, **33**, 2210158.
- 57 M. Yu, J. Yang, X. Zhang, M. Yuan, J. Zhang, L. Gao, J. Tang and X. Lan, *Adv. Mater.*, 2024, 2311830.
- 58 Y. Chen, C. Tan, Z. Wang, J. Miao, X. Ge, T. Zhao, K. Liao, H. Ge, Y. Wang, F. Wang, Y. Zhou, P. Wang, X. Zhou, C. Shan, H. Peng and W. Hu, *Sci. Adv.*, 2022, **8**, eabq1781.
- 59 Z. Dan, B. Yang, Q. Song, J. Chen, H. Li, W. Gao, L. Huang, M. Zhang, M. Yang, Z. Zheng, N. Huo, L. Han and J. Li, *ACS Appl. Mater. Interfaces*, 2023, **15**, 18101.
- 60 L. Tao, B. Yao, Q. Yue, Z. Dan, P. Wen, M. Yang, Z. Zheng, D. Luo, W. Fan, X. Wang and W. Gao, *Nanoscale*, 2021, **13**, 15403.
- 61 Q. Zhu, Y. Chen, X. Zhu, Y. Sun, Z. Cheng, J. Xu and M. Xu, *Sci. China Mater.*, 2023, **66**, 2777.
- 62 J. Mao, B. Zhang, Y. Shi, X. Wu, Y. He, D. Wu, J. Jie, C.-S. Lee and X. Zhang, *Adv. Funct. Mater.*, 2022, **32**, 2108174.
- 63 Y. Chen, Y. Zheng, J. Wang, X. Zhao, G. Liu, Y. Lin, Y. Yang, L. Wang, Z. Tang, Y. Wang, Y. Fang, W. Zhang and X. Zhu, *Sci. Adv.*, 2024, **10**, eadm9631.
- 64 B. Yin, X. Zhou, Y. Li, G. Hu, W. Wei, M. Yang, S. Jeong, W. Deng, B. Wu, Y. Cao, B. Huang, L. Pan, X. Yang, Z. Fu, Y. Fang, L. Shen, C. Yang, H. Wu, L. Lan, F. Huang, Y. Cao and C. Duan, *Adv. Mater.*, 2024, **36**, 2310811.

- 65 X. Chen, Y. Zhu, Y. Xu, M. Rao, P. Pang, B. Zhang, C. Xu, W. Ni, G. Li, J. Wu, M. Li, Y. Chen and Y. Geng, *Angew. Chem.*, 2024, e202413965.
- 66 Y. Wang, M. Yang, B. Yin, B. Wu, G. Liu, S. Jeong, Y. Zhang, C. Yang, Z. He, F. Huang, Y. Cao and C. Duan, *ACS Appl. Mater. Interfaces*, 2024, DOI: [10.1021/acsami.3c15365](https://doi.org/10.1021/acsami.3c15365).
- 67 M. Yang, B. Yin, G. Hu, Y. Cao, S. Lu, Y. Chen, Y. He, X. Yang, B. Huang, J. Li, B. Wu, S. Pang, L. Shen, Y. Liang, H. Wu, L. Lan, G. Yu, F. Huang, Y. Cao and C. Duan, *Chem.*, 2024, **10**, 1425.
- 68 Y. Zhang, J. Chen, J. Yang, M. Fu, Y. Cao, M. Dong, J. Yu, S. Dong, X. Yang, L. Shao, Z. Hu, H. Cai, C. Liu and F. Huang, *Adv. Mater.*, 2024, 2406950.
- 69 D. Ren, X. Meng, Z. Rong, M. Cao, A. C. Farrell, S. Somasundaram, K. M. Azizur-Rahman, B. S. Williams and D. L. Huffaker, *Nano Lett.*, 2018, **18**, 7901.
- 70 W.-J. Lee, P. Senanayake, A. C. Farrell, A. Lin, C.-H. Hung and D. L. Huffaker, *Nano Lett.*, 2016, **16**, 199.
- 71 S. Mauthe, Y. Baumgartner, M. Sousa, Q. Ding, M. D. Rossell, A. Schenk, L. Czornomaz and K. E. Moselund, *Nat. Commun.*, 2020, **11**, 4565.
- 72 J. W. Lee, D. Y. Kim, S. Baek, H. Yu and F. So, *Small*, 2016, **12**, 1328.
- 73 H. Yu, S. Liu, S. Baek, C. Dong and F. So, *J. Mater. Chem. C*, 2016, **4**, 11205.
- 74 E. Georgitzikis, P. E. Malinowski, J. Maes, A. Hadipour, Z. Hens, P. Heremans and D. Cheyns, *Adv. Funct. Mater.*, 2018, **28**, 1804502.
- 75 J. Lee, E. Georgitzikis, Y. Li, Z. Lin, J. Park, I. Lieberman, D. Cheyns, M. Jayapala, A. Lambrechts, S. Thijss, R. Stahl and P. E. Malinowski, 2020 IEEE International Electron Devices Meeting (IEDM), 2020, p. 16.
- 76 E. Georgitzikis, P. E. Malinowski, Y. Li, J. Maes, L. M. Hagelsieb, S. Guerrieri, Z. Hens, P. Heremans and D. Cheyns, *IEEE Sens. J.*, 2019, **20**, 6841.
- 77 J. H. Kim, V. Pejović, E. Georgitzikis, Y. Li, J. Kim, P. E. Malinowski, I. Lieberman, D. Cheyns, P. Heremans and J. Lee, *IEEE Trans. Electron Dev.*, 2022, **69**, 2900.
- 78 Y. Yuan, J.-L. Xu, J.-Y. Zhang, X. Gao, Y.-N. Zhong and S.-D. Wang, *IEEE Electron Dev. Lett.*, 2022, **43**, 1275.
- 79 M.-T. Jiang, Q. Yang, J.-L. Xu, Y. Yuan, J.-Y. Zhang, Y.-N. Zhong, X. Gao and S.-D. Wang, *Adv. Opt. Mater.*, 2023, **11**, 2202990.
- 80 J. Liu, P. Liu, D. Chen, T. Shi, X. Qu, L. Chen, T. Wu, J. Ke, K. Xiong, M. Li, H. Song, W. Wei, J. Cao, J. Zhang, L. Gao and J. Tang, *Nat. Electron.*, 2022, **5**, 443.
- 81 J. Liu, P. Liu, T. Shi, M. Ke, K. Xiong, Y. Liu, L. Chen, L. Zhang, X. Liang, H. Li, S. Lu, X. Lan, G. Niu, J. Zhang, P. Fei, L. Gao and J. Tang, *Nat. Commun.*, 2023, **14**, 5352.
- 82 Q. Xu, L. Meng, K. Sinha, F. I. Chowdhury, J. Hu and X. Wang, *ACS Photonics*, 2020, **7**, 1297.
- 83 J. Lee, E. Georgitzikis, Y. Hermans, N. Papadopoulos, N. Chandrasekaran, M. Jin, A. B. Siddik, F. De Roose, G. Uytterhoeven, J. H. Kim, R. Puybaret, Y. Li, V. Pejovic, G. Karve, D. Cheyns, J. Genoe, P. E. Malinowski, P. Heremans and K. Myny, *Nat. Electron.*, 2023, **6**, 590.
- 84 J. E. Murphy, M. C. Beard, A. G. Norman, S. P. Ahrenkiel, J. C. Johnson, P. Yu, O. I. Mićić, R. J. Ellingson and A. J. Nozik, *J. Am. Chem. Soc.*, 2006, **128**, 3241.
- 85 M. Grundmann, *Physics of semiconductors*, Springer, 2010, vol. 11.
- 86 V. Pejović, E. Georgitzikis, J. Lee, I. Lieberman, D. Cheyns, P. Heremans and P. E. Malinowski, *IEEE Trans. Electron Dev.*, 2021, **69**, 2840.
- 87 I. Moreels, K. Lambert, D. Smeets, D. De Muynck, T. Nollet, J. C. Martins, F. Vanhaecke, A. Vantomme, C. Delerue, G. Allan and Z. Hens, *ACS Nano*, 2009, **3**, 3023.
- 88 C. Dong, S. Liu, N. Barange, J. Lee, T. Pardue, X. Yi, S. Yin and F. So, *ACS Appl. Mater. Interfaces*, 2019, **11**, 44451.
- 89 C. Gréboval, A. Chu, N. Goubet, C. Livache, S. Ithurria and E. Lhuillier, *Chem. Rev.*, 2021, **121**, 3627.
- 90 E. Izquierdo, A. Robin, S. Keuleyan, N. Lequeux, E. Lhuillier and S. Ithurria, *J. Am. Chem. Soc.*, 2016, **138**, 10496.
- 91 N. Goubet, A. Jagtap, C. Livache, B. Martinez, H. Portale, X. Z. Xu, R. P. Lobo, B. Dubertret and E. Lhuillier, *J. Am. Chem. Soc.*, 2018, **140**, 5033.
- 92 T. Apretna, N. Nilforoushan, J. Tignon, S. Dhillon, F. Carosella, R. Ferreira, E. Lhuillier and J. Mangeney, *Appl. Phys. Lett.*, 2022, **121**, 251101.
- 93 X. Lan, M. Chen, M. H. Hudson, V. Kamysbayev, Y. Wang, P. Guyot-Sionnest and D. V. Talapin, *Nat. Mater.*, 2020, **19**, 323.
- 94 M. Chen, X. Xue, T. Qin, C. Wen, Q. Hao and X. Tang, *Adv. Mater. Technol.*, 2023, **8**, 2300315.
- 95 K. A. Sergeeva, H. Zhang, A. S. Portniagin, E. Bossavit, G. Mu, S. V. Kershaw, S. Ithurria, P. Guyot-Sionnest, S. Keuleyan, C. Delerue, X. Tang, A. L. Rogach and E. Lhuillier, *Adv. Funct. Mater.*, 2024, 2405307.
- 96 Y. Tian, H. Luo, M. Chen, C. Li, S. V. Kershaw, R. Zhang and A. L. Rogach, *Nanoscale*, 2023, **15**, 6476.
- 97 X. Tang, M. M. Ackerman, M. Chen and P. Guyot-Sionnest, *Nat. Photonics*, 2019, **13**, 277.
- 98 Y. Wang, L. Peng, J. Schreier, Y. Bi, A. Black, A. Malla, S. Goossens and G. Konstantatos, *Nat. Photonics*, 2024, **18**, 236.
- 99 M. P. Hendricks, M. P. Campos, G. T. Cleveland, I. Jen-La Plante and J. S. Owen, *Science*, 2015, **348**, 1226.
- 100 J. Zhang, J. Gao, E. M. Miller, J. M. Luther and M. C. Beard, *ACS Nano*, 2014, **8**, 614.
- 101 M. A. Hines and G. D. Scholes, *Adv. Mater.*, 2003, **15**, 1844.
- 102 X. Wang, J. Zhuang, Q. Peng and Y. Li, *Nature*, 2005, **437**, 121.
- 103 H. Wu and Z. Ning, *J. Appl. Phys.*, 2023, **133**, 041101.
- 104 S. Chan, M. Liu, K. Latham, M. Haruta, H. Kurata, T. Teranishi and Y. Tachibana, *J. Mater. Chem. C*, 2017, **5**, 2182.
- 105 S. Kahmann and M. A. Loi, *Appl. Phys. Rev.*, 2020, **7**, 041305.
- 106 P. B. Green, P. Narayanan, Z. Li, P. Sohn, C. J. Imperiale and M. W. Wilson, *Chem. Mater.*, 2020, **32**, 4083.
- 107 D. V. Talapin, A. L. Rogach, M. Haase and H. Weller, *J. Phys. Chem. B*, 2001, **105**, 12278.

- 108 Y. Wang, K. Lu, L. Han, Z. Liu, G. Shi, H. Fang, S. Chen, T. Wu, F. Yang, M. Gu, S. Zhou, X. Ling, X. Tang, J. Zheng, M. A. Loi and W. Ma, *Adv. Mater.*, 2018, **30**, 1704871.
- 109 H. Fu, S.-W. Tsang, Y. Zhang, J. Ouyang, J. Lu, K. Yu and Y. Tao, *Chem. Mater.*, 2011, **23**, 1805.
- 110 I. Moreels, Y. Justo, B. De Geyter, K. Haustraete, J. C. Martins and Z. Hens, *ACS Nano*, 2011, **5**, 2004.
- 111 Y. Wang, Z. Liu, N. Huo, F. Li, M. Gu, X. Ling, Y. Zhang, K. Lu, L. Han, H. Fang, A. G. Shulga, Y. Xue, S. Zhou, F. Yang, X. Tang, J. Zheng, M. A. Loi, G. Konstantatos and W. Ma, *Nat. Commun.*, 2019, **10**, 5136.
- 112 J. Jean, J. Xiao, R. Nick, N. Moody, M. Nasilowski, M. Bawendi and V. Bulović, *Energy Environ. Sci.*, 2018, **11**, 2295.
- 113 Y. Liu, Y. Gao, Q. Yang, G. Xu, X. Zhou, G. Shi, X. Lyu, H. Wu, J. Liu, S. Fang, M. I. Ullah, L. Song, K. Lu, M. Cao, Q. Zhang, T. Li, J. Xu, S. Wang, Z. Liu and W. Ma, *Angew. Chem., Int. Ed.*, 2023, **62**, e202300396.
- 114 P. R. Brown, D. Kim, R. R. Lunt, N. Zhao, M. G. Bawendi, J. C. Grossman and V. Bulovic, *ACS Nano*, 2014, **8**, 5863.
- 115 O. Voznyy, D. Zhitomirsky, P. Stadler, Z. Ning, S. Hoogland and E. H. Sargent, *ACS Nano*, 2012, **6**, 8448.
- 116 D. Bozyigit, W. M. Lin, N. Yazdani, O. Yarema and V. Wood, *Nat. Commun.*, 2015, **6**, 6180.
- 117 S. Volk, N. Yazdani, O. Yarema, M. Yarema and V. Wood, *ACS Appl. Electron. Mater.*, 2020, **2**, 398.
- 118 S. Volk, N. Yazdani and V. Wood, *J. Phys. Chem. Lett.*, 2020, **11**, 9255.
- 119 D. Bozyigit, S. Volk, O. Yarema and V. Wood, *Nano Lett.*, 2013, **13**, 5284.
- 120 P. Nagpal and V. I. Klimov, *Nat. Commun.*, 2011, **2**, 486.
- 121 C. R. Kagan, *Chem. Soc. Rev.*, 2019, **48**, 1626.
- 122 A. J. Houtepen, Z. Hens, J. S. Owen and I. Infante, *Chem. Mater.*, 2017, **29**, 752.
- 123 C. Giansante and I. Infante, *J. Phys. Chem. Lett.*, 2017, **8**, 5209.
- 124 O. Voznyy, S. Thon, A. Ip and E. Sargent, *J. Phys. Chem. Lett.*, 2013, **4**, 987.
- 125 D. Zhrebetskyy, Y. Zhang, M. Salmeron and L.-W. Wang, *J. Phys. Chem. Lett.*, 2015, **6**, 4711.
- 126 R. H. Gilmore, Y. Liu, W. Shcherbakov-Wu, N. S. Dahod, E. M. Lee, M. C. Weidman, H. Li, J. Jean, V. Bulović, A. P. Willard, J. C. Grossman and W. A. Tisdale, *Matter*, 2019, **1**, 250.
- 127 G. Shi, H. Wang, Y. Zhang, C. Cheng, T. Zhai, B. Chen, X. Liu, R. Jono, X. Mao, Y. Liu, X. Zhang, X. Ling, Y. Zhang, X. Meng, Y. Chen, S. Duham, L. Zhang, T. Li, L. Wang, S. Xiong, T. Sagawa, T. Kubo, H. Segawa, Q. Shen, Z. Liu and W. Ma, *Nat. Commun.*, 2021, **12**, 4381.
- 128 N. Yazdani, S. Andermatt, M. Yarema, V. Farto, M. H. Bani-Hashemian, S. Volk, W. M. Lin, O. Yarema, M. Luisier and V. Wood, *Nat. Commun.*, 2020, **11**, 2852.
- 129 L. K. Vandamme, X. Li and D. Rigaud, *IEEE Trans. Electron Dev.*, 1994, **41**, 1936.
- 130 A. Rehman, J. A. D. Notario, J. S. Sanchez, Y. M. Meziani, G. Cywiński, W. Knap, A. A. Balandin, M. Levinstein and S. Rumyantsev, *Nanoscale*, 2022, **14**, 7242.
- 131 D. Wolf and E. Holler, *J. Appl. Phys.*, 1967, **38**, 189.
- 132 S. Ghosh, D. H. Mudiyanselage, S. Rumyantsev, Y. Zhao, H. Fu, S. Goodnick, R. Nemanich and A. A. Balandin, *Appl. Phys. Lett.*, 2023, **122**, 212109.
- 133 B. C. Lee, Y. Seo, C. Kim, Y. Kim, M.-K. Joo and G.-T. Kim, *Appl. Phys. Lett.*, 2022, **120**, 253507.
- 134 Y. Fang, A. Armin, P. Meredith and J. Huang, *Nat. Photonics*, 2019, **13**, 1.
- 135 V. Arkhipov, U. Wolf and H. Bässler, *Phys. Rev. B: Condens. Matter Mater. Phys.*, 1999, **59**, 7514.
- 136 W. F. Pasveer, J. Cottaar, C. Tanase, R. Coehoorn, P. A. Bobbert, P. W. M. Blom, D. M. de Leeuw and M. A. J. Michels, *Phys. Rev. Lett.*, 2005, **94**, 206601.
- 137 J. Kublitski, A. Hofacker, B. K. Boroujeni, J. Benduhn, V. C. Nikolis, C. Kaiser, D. Spoltore, H. Kleemann, A. Fischer, F. Ellinger, K. Vandewal and K. Leo, *Nat. Commun.*, 2021, **12**, 551.
- 138 B. L. Williams, S. Smit, B. J. Kniknie, K. J. Bakker, W. Keuning, W. Kessels, R. E. Schropp and M. Creatore, *Prog. Photovoltaics*, 2015, **23**, 1516.
- 139 M. Padilla, B. Michl, B. Thaidigsmann, W. Warta and M. C. Schubert, *Sol. Energy Mater. Sol. Cells*, 2014, **120**, 282.
- 140 W. Shockley and H. J. Queisser, *J. Appl. Phys.*, 1961, **32**, 510.
- 141 K. Vandewal, K. Tvingstedt, J. V. Manca and O. Inganäs, *IEEE J. Sel. Top. Quantum Electron.*, 2010, **16**, 1676.
- 142 J. Yang, Y. Lv, Z. He, B. Wang, S. Chen, F. Xiao, H. Hu, M. Yu, H. Liu, X. Lan, H.-Y. Hsu, H. Song and J. Tang, *ACS Photonics*, 2023, **10**, 2226.
- 143 J. W. Lee, D. Y. Kim and F. So, *Adv. Funct. Mater.*, 2015, **25**, 1233.
- 144 J. Choi, J. W. Jo, F. P. G. de Arquer, Y.-B. Zhao, B. Sun, J. Kim, M.-J. Choi, S.-W. Baek, A. H. Proppe, A. Seifitokaldani, D.-H. Nam, P. Li, O. Ouellette, Y. Kim, O. Voznyy, S. Hoogland, S. O. Kelley, Z.-H. Lu and E. H. Sargent, *Adv. Mater.*, 2018, **30**, 1801720.
- 145 X. Xiao, K. Xu, M. Yin, Y. Qiu, W. Zhou, L. Zheng, X. Cheng, Y. Yu and Z. Ning, *Appl. Phys. Lett.*, 2020, **116**, 101102.
- 146 L. Chen, J. Liu, P. Liu, S. Lu, Y. Yang, X. Liang, L. Zhang, J. Hu, J. Yang, Y. Liu, W. Ma, X. Zhao, X. Lan, J. Zhang, L. Gao and J. Tang, *ACS Photonics*, 2023, **10**, 2374.
- 147 Y. Di, K. Ba, Y. Chen, X. Wang, M. Zhang, X. Huang, Y. Long, M. Liu, S. Zhang, W. Tang, Z. Huang, T. Lin, H. Shen, X. Meng, M. Han, Q. Liu and J. Wang, *Adv. Sci.*, 2024, **11**, 2307169.
- 148 J. Yang, J. Lee, J. Lee and W. Yi, *ACS Appl. Mater. Interfaces*, 2018, **10**, 25311.
- 149 H. K. Woo, M. S. Kang, T. Park, J. Bang, S. Jeon, W. S. Lee, J. Ahn, G. Cho, D.-K. Ko, Y. Kim, D.-H. Hab and S. J. Oh, *Nanoscale*, 2019, **11**, 17498.
- 150 M. Graetzel, R. A. Janssen, D. B. Mitzi and E. H. Sargent, *Nature*, 2012, **488**, 304.
- 151 S. Ahn, T.-H. Han, K. Maleski, J. Song, Y.-H. Kim, M.-H. Park, H. Zhou, S. Yoo, Y. Gogotsi and T.-W. Lee, *Adv. Mater.*, 2020, **32**, 2000919.
- 152 C. Venettacci, B. Martn-Garcia, M. Prato, I. Moreels and A. De Iacovo, *Nanotechnology*, 2019, **30**, 405204.

- 153 M. Sulaman, S. Yang, A. Bukhtiar, P. Tang, Z. Zhang, Y. Song, A. Imran, Y. Jiang, Y. Cui, L. Tang and B. Zou, *Adv. Funct. Mater.*, 2022, **32**, 2201527.
- 154 J. He, K. Qiao, L. Gao, H. Song, L. Hu, S. Jiang, J. Zhong and J. Tang, *ACS Photonics*, 2014, **1**, 936.
- 155 F. P. Garca de Arquer, T. Lasanta, M. Bernechea and G. Konstantatos, *Small*, 2015, **11**, 2636.
- 156 K. Qiao, Y. Cao, X. Yang, J. Khan, H. Deng, J. Zhang, U. Farooq, S. Yuan and H. Song, *RSC Adv.*, 2017, **7**, 52947.
- 157 C. Liu, K. Wang, P. Du, E. Wang, X. Gong and A. J. Heeger, *Nanoscale*, 2015, **7**, 16460.
- 158 J.-Y. Zhang, J.-L. Xu, T. Chen, X. Gao and S.-D. Wang, *ACS Appl. Mater. Interfaces*, 2019, **11**, 44430.
- 159 M. M. Ackerman, M. Chen and P. Guyot-Sionnest, *Appl. Phys. Lett.*, 2020, **116**, 083502.
- 160 J. Yang, H. Hu, Y. Lv, M. Yuan, B. Wang, Z. He, S. Chen, Y. Wang, Z. Hu, M. Yu, X. Zhang, J. He, J. Zhang, H. Liu, H.-Y. Hsu, J. Tang, H. Song and X. Lan, *Nano Lett.*, 2022, **22**, 3465.
- 161 R. Guo, J. Meng, W. Lin, A. Liu, T. Pullerits, K. Zheng and J. Tian, *Chem. Eng. J.*, 2021, **403**, 126452.
- 162 S. Arya, Y. Jiang, B. K. Jung, Y. Tang, T. N. Ng, S. J. Oh, K. Nomura and Y.-H. Lo, *Nano Lett.*, 2023, **23**, 9943.